Static source properties of slow and fast earthquakes

Priyamvada Nanjundiah[1,2], Sylvain Barbot[3], Shengji Wei[1,2]

[1]Earth Observatory of Singapore, 50 Nanyang Avenue, Blk N2.1-01a-15, Nanyang Technological University, Singapore

[2]Asian School of the Environment, 50 Nanyang Avenue, Blk N2.1-01a,Nanyang Technological University, Singapore

[3]Department of Earth Sciences, University of Southern California, Los Angeles, CA 90089-0740, USA

Key Points:

- We compile finite slip distributions for slow and fast earthquakes to quantify static source properties.
- The potency density varies systematically with rupture style, tectonic setting, and centroid depth.
- The moment-duration scaling of slow-slip events is affected by large variability in potency density.

Corresponding author: Priyamvada Nanjundiah, priyamvada.n@gmail.com

Abstract

The source characteristics of slow and fast earthquakes provide a window into the mechanical properties of faults. In particular, the average stress drop controls the evolution of friction, fault slip, and event magnitude. However, this important source property is typically inferred from the analysis of seismic waves and is subject to many epistemic uncertainties. Here, we investigate the source properties of 52 earthquakes and 17 slow-slip events on thrust and strike-slip faults in various tectonic settings using slip distributions constrained by geodesy in combination with other data. We determine the width, potency, and potency density of slow and fast earthquake source based on static slip distributions. The potency density, defined conceptually as the ratio of average slip to rupture radius, is a measure of anelastic deformation with limited bias from rigidity differences across depths and tectonic settings. Strike-slip earthquakes have the highest potency density, varying from 20 to 500 microstrain, with no discernible trend. The potency density is on average lower on continental thrust faults and megathrusts, from 10 to 200 microstrain, with an algebraic decrease with centroid depth, indicative of systematic changes in dominant rupture processes with depth. Slow slip events represent an end-member style of rupture with low potency density and large rupture width. Significant variability in potency density of slow-slip event affects their moment-duration scaling. The variations of source properties across tectonic settings, depth, and rupture styles can be used to better constrain numerical simulations of seismicity and to assess the source characteristics of future earthquakes and slow slip events.

Plain Language Summary

Natural earthquakes reduce the stress that accumulates on faults due to plate tectonics. To better understand the variability of seismic hazards around active faults, we survey the properties of slow and fast earthquakes around the world. The potential of faults to concentrate large slip in the rupture area differs depending on the geological setting, the depth of the source, and the type of rupture. Earthquakes in a continental setting condense more slip in a given rupture area, particularly in transform faults like the San Andreas fault. Subduction zone earthquakes, although some of the largest events on Earth, generally distribute less slip over a wider area, but this varies as a function of depth. Slow earthquakes represent an extreme case of little slip distributed over a large area. The

propensity of rupture characteristics to vary with fault type and depth may help forecast the hazards posed by future seismicity.

1 Introduction

The earthquake phenomenon includes a wide spectrum of rupture styles associated with different source characteristics (Beroza & Ide, 2011; Obara & Kato, 2016; Veedu & Barbot, 2016; Leeman et al., 2016; Scuderi et al., 2017; Barbot, 2019b). The stress change on a fault produced by an earthquake is one of the fundamental physical properties that govern the seismic cycle, impacting the style of rupture, i.e., slow or fast earthquake, and the magnitude of the event (Aki, 1967, 1979; Kanamori & Anderson, 1975; Kanamori et al., 1993; Venkataraman & Kanamori, 2004; Ye et al., 2016a; Poli & Prieto, 2016). The scaling relationship between stress drop and various other source parameters depends on the tectonic setting (e.g., Scholz et al., 1986; Walsh & Watterson, 1988; Romanowicz, 1992) and on the rupture style (N. Beeler et al., 2001; Liu-Zeng et al., 2005; Peng & Gomberg, 2010; Kato, 2012; Gomberg et al., 2016; Cocco et al., 2016; Cattania & Segall, 2018). Current estimates of stress drop for fast earthquakes typically rely on seismological data, whereby the corner frequency of the source moment-rate function provides rupture duration (e.g., Allmann & Shearer, 2009; Shearer et al., 2006; Vallée, 2013; Ye et al., 2016b; Courboulex et al., 2016) and a theoretical model is used to estimate an effective rupture length (Brune, 1970; Madariaga, 1976, 1977; Kaneko & Shearer, 2014). However, stress drop estimates based on seismological approaches are subject to large uncertainties (Prieto et al., 2006; Baltay et al., 2011), for example, due to trade-offs between rupture velocity and rise time, the amplitude of high-frequency waves and attenuation (Baltay & Hanks, 2014), and between the rupture velocity and the overall slip area. Additional bias, especially for large events, may also arise from overly simplifying assumptions about the rupture process including directivity, single versus multi-pulse ruptures, geometry (Kaneko & Shearer, 2015), estimation of the overall duration of the event (Courboulex et al., 2016) and unknown variations in elastic properties of the surrounding rocks.

To mitigate these issues, we consider finite slip distributions of slow and fast earthquakes constrained by geodetic data, along with other measurements. Inversion of geodetic data for the spatial distribution of slip on a fault is also subject to fundamental limitations, notably due to the St-Venant principle that implies a decreasing resolution with increasing distance between source and observa-

tions. However, the deployment of increasingly large and dense geodetic observatories, the development of better analytic standards in inverse theory (Yabuki & Matsu'ura, 1992; Fukahata & Wright, 2008; Aster et al., 2012; Funning et al., 2014; Nocquet, 2018; Hang et al., 2020), and the joint inversion of complementary datasets, both geodetic and seismological, has increased the accuracy of slip distributions (McGuire & Segall, 2003; Atzori & Antonioli, 2011; Evans & Meade, 2012; Barbot et al., 2013; Duputel et al., 2014; Minson et al., 2014; Sathiakumar et al., 2017; DeVries et al., 2017; Gombert et al., 2017, 2018; Amey et al., 2018). For example, the large uncertainties associated with shallow slip near the trench during the 2011 Mw=9.1 Tohoku, Japan earthquake were largely reduced by considering tsunami data (e.g., Yamazaki et al., 2011; Bletery et al., 2014; J. Jiang & Simons, 2016). Rupture of subduction megathrusts can also be well imaged by combining high-rate Global Positioning System (GPS), teleseismic body waves, synthetic aperture radar interferometry (InSAR), campaign GPS, and tsunami observations (Yue, Lay, Rivera, An, et al., 2014). The slip distribution of continental earthquakes is increasingly well resolved by space geodetic observations, notably as InSAR can constrain the three-dimensional surface displacement with high spatial resolution (Fialko et al., 2001; Fialko, 2004; Fialko et al., 2005; Bechor & Zebker, 2006; Barbot et al., 2008a; Avouac et al., 2015; T. Wang & Jónsson, 2015; Moore et al., 2017; T. Wang, Wei, et al., 2018; T. Wang, Shi, et al., 2018; Z. Wang et al., 2018).

Geodetic-based slip distributions of slow and fast earthquakes may constrain the geometric properties of ruptures, i.e., the effective length, width, and area (e.g., Weston et al., 2012; Brengman et al., 2019), but a remaining issue regarding stress drop is large variations of elastic properties across tectonic settings and source depths. The variability of elastic properties should be accounted for to compare estimates of stress drop for events in different tectonic settings or depth, but the elastic properties are not always well known. Following the previous suggestion of quantifying the size of earthquakes with the seismic potency $P = As$ instead of the seismic moment $M = GAs$ (Ben-Zion, 2001; Ben-Zion & Zhu, 2002), where G is the rigidity, A is the rupture area, and s is the representative fault slip, we propose to look at the average potency density of the rupture. We define potency density as an extrinsic property of ruptures that represents a characteristic strain, defined as the ratio of fault slip to rupture length

$$\epsilon = c\,\frac{s}{R}\ , \tag{1}$$

where R is a characteristic length scale such that $A = R^2$ and $c \sim 1$ is a non-dimensional constant controlled by geometry. That strain corresponds to a potency density becomes evident when considering the relationship with seismic potency, i.e. $P \propto \epsilon R^3$ or $\epsilon \propto P/R^3$. Our definition therefore differs from that of Ben-Zion et al. (2003) and Ben-Zion and Lyakhovsky (2019) that refer to the local potency per unit volume as an intrinsic property. As a suitable alternative to the potency density defined in equation (1), Vallée (2013) uses the term strain drop to refer to the same quantity. But the name may be ambiguous because as elastic strain indeed decreases around a rupture, anelastic strain in fact accrues.

A dimensional analysis shows that the recurrence time of instabilities is controlled by potency density, as in $T_r \propto \epsilon R/V_{\mathrm{L}}$, where V_{L} is the fault long-term loading rate. The potency density is also related to the static stress drop, following

$$\Delta\tau = 2G\epsilon \ , \tag{2}$$

where the factor of 2 comes from Hooke's law in three dimensions. Hence, the potency density provides a useful source property relevant to both slow and fast earthquakes that can be estimated from static slip distributions with limited bias from unknown variations in elastic properties.

In this study, we build a curated catalog of slip distributions based on the analysis of geodetic and other geophysical data for thrust fault and megathrust earthquakes (25 events), strike-slip fault earthquakes (27 events), and slow-slip events on subduction megathrusts (17 events), adding to 65 events (Figure 1). The slip distributions are obtained from a long legacy of published work (62 events) and original results (3 events) for the 2015 Mw 7.2 Lake Sarez (Tajikistan), 2018 Palu (Indonesia), and 2019 Ridgecrest (California) earthquakes. Unfortunately, not enough data are available to characterize normal faulting events. In Section 2, we describe the methodology to derive the width, potency, and potency density automatically from the finite slip distributions. In Section 3, we present the catalog and the relationships among source characteristics. We find that the down-dip rupture extent of slow and fast earthquakes increases with centroid depth. Notably, the potency density of subduction earthquakes seems to decrease algebraically with depth, indicating that different rupture

processes operate at different depths. We also discuss the impact of potency density on the moment-duration scaling relationship of slow-slip events.

2 Static source properties from finite slip distributions

We seek a systematic approach to analyze a large number of slip distributions that have in common a complex source geometry, including non-uniform slip distribution, several branches of varying strike and dip, and rake variations. For a circular patch of radius R with uniform slip s, the potency density finds a closed-form expression (Eshelby, 1957)

$$\epsilon = \frac{7\pi}{32}\frac{s}{R} \ . \tag{3}$$

Some authors (e.g., Somerville et al., 1999; Barbot et al., 2009; Brown et al., 2015) estimate the effective radius and the mean slip in finite slip distributions to approximate the potency or the stress drop using equations (2) and (3). Mai and Beroza (2000) first estimate rupture dimensions and then estimate an average slip that conserves the total seismic moment. These approaches are problematic in our case because they either rely on arbitrary slip thresholds to define the slip area, ignore the geometrical intricacies of ruptures, or cannot address the issues associated with multiple fault strands. A single slip threshold is not applicable to treat a catalog of events with magnitudes range from Mw=6.0 to 9.5.

We propose an estimate of the potency density that can be applied to realistic slip distributions with multiple fault strands, rake rotations, and possibly non-planar faults. Consider a fault surface $\partial\Omega$ with varying normal vector $\hat{\boldsymbol{n}}$ associated with a slip distribution $\boldsymbol{s}$. The deformation of the surrounding rocks leads to a distribution of strain $\boldsymbol{\epsilon}$ in the elastic medium. Strain is a symmetric, second-order tensor. To reduce the tensor field to a scalar quantity, we seek an average of the strain components aligned with the shear dislocation defined by the dyadic product $\hat{\boldsymbol{n}} \otimes \hat{\boldsymbol{s}}$ along the fault (Barbot & Fialko, 2010), where the hat indicates a unit vector, such that $\boldsymbol{s} = s\,\hat{\boldsymbol{s}}$, with $s \geq 0$. Following the estimates of stress drop based on energy considerations proposed by Noda et al. (2013), we use

a weighted average of the strain components based on slip,

$$\epsilon = -\frac{\int_{\partial\Omega} \boldsymbol{\epsilon} : (\hat{\boldsymbol{n}} \otimes \boldsymbol{s}) \, \mathrm{d}A}{\int_{\partial\Omega} s \, \mathrm{d}A} \, , \tag{4}$$

where the symbol : is the double-dot product (Nemat-Nasser & Hori, 1999; Nemat-Nasser, 2004). The estimate of potency density in equation (4) can be obtained without imposing any arbitrary thresholds on rupture area or slip and is applicable to any slip distribution regardless of complexity. The formulation also accounts for rake rotations and is independent of rigidity. Since slip is used as a weighting factor, the fault area devoid of slip are naturally excluded. This process is illustrated in Figure 2 using the slip distribution of the 2015 Mw 7.2 Lake Sarez earthquake, which was obtained by inversion of SAR data and teleseismic body waves. The slip distribution features varying strike, dip, and rake along the rupture (Figure 2a). The strain distribution on the fault plane, computed as $\boldsymbol{\epsilon} : (\hat{\boldsymbol{n}} \otimes \hat{\boldsymbol{s}})$, is shown in Figure 2b. Most areas of positive strain change are associated with regions of little to no slip and are weighted out. Meanwhile, the areas of smooth slip distribution that would be difficult to outline with a slip threshold, for example to the southwest, are associated with little strain, contributing minimally to the overall potency density estimation. The method can then be applied uniformly to events of various sizes. When treating the entire catalog of events, we consider finite slip distributions with fault surfaces decomposed into rectangular or triangular meshes. We calculate the strain tensor at the patch centers assuming a uniform half-space with Poisson's ratio $\nu = 0.25$ using the analytical solution of Okada (1992) for rectangular dislocations and the one of Nikkhoo and Walter (2015) for triangular dislocations. If the elastic properties are uniform, the deformation does not depend on the rigidity. When calculating potency density, we ignore vertical or lateral variations of elastic moduli.

In the same vein, we seek to describe the geometrical properties of ruptures from finite slip distributions without potential bias from arbitrary thresholds for slip, such that slow and fast, small and large earthquakes can be treated consistently. The definition of rupture width can vary depending on the data considered. Rupture length can be estimated from surface slip (Wyss, 1979; Manighetti et al., 2001, 2007), or from the spatial extent of early aftershocks (Kanamori & Anderson, 1975; Darragh & Bolt, 1987), leading to different results (Wells & Coppersmith, 1994). We use slip as a weight-

ing factor and estimate the centroid location as follows

$$\bar{z} = \frac{\int_{\partial\Omega} z\, s \,\mathrm{d}A}{\int_{\partial\Omega} s \,\mathrm{d}A} \ , \tag{5}$$

where $\bar{z}$ is the centroid depth, and z is the depth of the fault surface. To facilitate the comparison of ruptures occurring on faults with different dip angles, we focus on the depth extent of ruptures instead of the down-dip rupture width. On quasi-vertical strike-slip faults, comparing the depth extent or the down-dip extent is equivalent. On shallow dipping faults, considering the depth extent is useful to understand the potential relationship between rupture geometry and stratigraphy or the overall vertical thermo-mechanical structure of the plate boundary. To estimate the rupture width in the depth direction, we treat rupture depth as a random variable. We do not make any specific assumption about the probability density distribution of depth, except for the fact that it is a positive quantity, and therefore a Gaussian distribution is not appropriate, unavoidably predicting non-zero probability of negative depths (Tarantola, 2004). To avoid this issue, we manipulate the logarithm of depth. For example, if the logarithm of depth was normally distributed, then depth would be log-normally distributed, predicting zero probability of slip above the surface. Accordingly, we first compute another estimate of the centroid depth as

$$\begin{aligned} \bar{w} &= \log_{10}\left(\bar{z}^*\right) \\ &= \frac{\int_{\partial\Omega} \log_{10}(z)\, s \,\mathrm{d}A}{\int_{\partial\Omega} s \,\mathrm{d}A} \ , \end{aligned} \tag{6}$$

where $\log_{10}(x) = \log(x)/\log(10)$. We then estimate the standard deviation of the depth distribution

$$\bar{\sigma}^2 = \frac{\int_{\partial\Omega} \left[\log_{10}\left(z\right) - \bar{w}\right]^2 s \,\mathrm{d}A}{\int_{\partial\Omega} s \,\mathrm{d}A} \ . \tag{7}$$

Finally, we define the rupture width in the depth direction as the range of depths that would encompass more than 98% of the slip distribution is depth was log-normally distributed, i.e., $W = 10^{\bar{w}+\bar{\sigma}} - 10^{\bar{w}-\bar{\sigma}}$. Simplifying this expression, we obtain

$$W = 2\,\bar{z}^* \sinh(\sigma \log(10)) \ . \tag{8}$$

These estimates can accommodate non-planar faults, multiple strands, and non-uniform slip distributions. The estimates of rupture dimension and potency density are independent beyond the fact that they use the same slip distribution.

3 Source characteristics of earthquakes and slow-slip events

We compile a collection of finite slip distributions for slow and fast earthquakes based on the analysis of geodetic and other geophysical data (Figure 1). We curate a catalog based on the dataset used to constrain the models, the quality of the inversion procedure, in particular whether an objective criterion is used for the degree of regularization, and the absence of unrealistic features like spurious slip concentration at the boundary of the discretized fault. We collect published slip distributions for 52 earthquakes and 17 slow-slip events and combine them in a uniform format where the slip, position, length, width, strike, dip, and rake is documented for every rectangular patch, and additionally the vertex coordinates for triangular dislocations. The database includes 27 strike-slip fault earthquakes, 25 thrust fault and megathrust earthquakes, and 13 megathrust slow-slip events. The catalog includes strike-slip fault earthquakes from moment magnitude Mw=6.0 to 8.6 and thrust earthquakes from magnitude Mw=6.3 to 9.2.

All models are constrained by geodetic data, i.e., GPS and/or InSAR, but may also include regional and teleseismic data and tsunami records. In some cases, only one model satisfies the requirements and can be found in digital form. However, in many cases, the same event is documented in several studies. Collectively, the 65 events considered here are documented in at least 109 different models. For example, several sophisticated models of the 1992 Mw=7.3 Landers, California earthquake based on seismic and geodetic data can be found (e.g., Hernandez et al., 1999; Wald & Heaton, 1994), but we prefer the model of Fialko (2004) based on a reconstruction of the three-dimensional surface displacements at high spatial resolution. The surface displacements of the 2010 Mw=7.2 El Mayor-Cucapah earthquake was constrained by InSAR data (M. Wei et al., 2011), but the model of S. Wei et al. (2013) includes teleseismic and regional seismic data, improving resolution at depth. Similarly, the 1999 Mw=7.1 Hector Mine earthquake was constrained with geodesy (Simons, 2002), but the model of Salichon et al. (2004) includes InSAR, GPS, and teleseismic data. Model selection has an important impact on the estimation of potency density. For the Hector Mine earthquake, the models of Simons

(2002) and Salichon et al. (2004) imply a potency density of 168 and 259 microstrain, respectively. For the Parkfield earthquake, the models of Ji et al. (2004), Dreger et al. (2005), and Barbot et al. (2012) imply potency densities of 45, 22, and 33 microstrain, respectively. This indicates that the epistemic uncertainties associated with model discretization, data selection, and inversion methods are multiplicative. The variability found in multiple models of the same event indicates that the potency density is well constrained within a factor of two. Although these estimates may vary significantly within that range, these differences pale in regard to the overall variability of potency density across strike-slip fault earthquakes, from 20 to 500 microstrain, covering about two orders of magnitude. Among strike-slip fault earthquakes, we find that model selection has no impact on the relationships among source characteristics, as there is no systematic variation of potency density with depth or magnitude for this type of event.

The source properties of subduction megathrust earthquakes are more sensitive to model selection due to the various assumptions affecting shallow slip near the trench (e.g., Loveless & Meade, 2011). In particular, a prevailing, but incorrect assumption has been that fault slip in the accretionary region is aseismic. However, accretionary prisms are known to produce tsunami earthquakes (Kanamori, 1972; Pelayo & Wiens, 1992; Satake & Tanioka, 1999; Bilek & Lay, 2002; Geersen, 2019), the rupture of giant earthquakes often reaches the trench (e.g., Ishii et al., 2005; Lorenzo-Martín et al., 2006; Fujiwara et al., 2011; Yue, Lay, Rivera, An, et al., 2014; Tomita et al., 2017), and low-frequency earthquakes and tectonic tremors occur at shallow depth at subduction zones (Y. Jiang et al., 2012; Dixon et al., 2014; Wallace et al., 2016, 2017; Toh et al., 2018; Nakano et al., 2018). Among the slip distributions of giant earthquakes, i.e., the 2004 Mw=9.2 Sumatra-Andaman (Indonesia), 2011 Mw=9.1 Tohoku-Oki (Japan), and 2010 Mw=8.8 Maule (Chile) earthquakes (Rhie et al., 2007; Chlieh et al., 2007; Simons et al., 2012; Lorito et al., 2011; Luttrell et al., 2011; S. Wei et al., 2012; Iinuma et al., 2012) and tsunami earthquakes (Newman, Hayes, et al., 2011; Bilek et al., 2011; Satake et al., 2013; Yue, Lay, Rivera, Bai, et al., 2014), we select those that mitigate uncertainty in shallow slip by incorporating geodetic measurements with tsunami and other geophysical data. Even with these restrictions, the epistemic uncertainties associated with meshing, regularization and data selection introduce large variability in source characteristics. For example, the models of S. Wei et al. (2012), Yamazaki et al. (2011), and Bletery et al. (2014) for the 2011 Mw=9.1 Tohoku-Oki earthquake im-

ply a potency density of 51, 102, and 160 microstrain, respectively and a centroid depth of 18, 14, and 7 km, respectively. These source characteristics are also well constrained within a factor of two. However, given the range of potency density from 10 to 200 microstrain and of centroid depths from 2 to 50 km among thrust earthquakes, these uncertainties do not significantly affect the overall depth dependence of potency density for this type of events.

For each finite slip distribution of slow and fast earthquakes, we estimate the width in the depth direction, potency, and potency density. The supplementary materials include the slip distributions in a uniform format and the estimated source characteristics for all published models available. When multiple slip models are available, we select the one from the most comprehensive study. The source characteristics are listed in Table 1 for strike-slip earthquakes, Table 2 for thrust and megathrust earthquakes, and Table 3 for megathrust slow-slip events. We cluster the events in groups of broadly similar tectonic settings, including strike-slip faults, thrust faults, and megathrusts. We further identify the tsunamigenic earthquakes, which include any earthquake that generated a substantial tsunami, encompassing the so-called tsunami earthquakes that generate a tsunami larger than what would be anticipated for their magnitude (Kanamori, 1972).

The source characteristics of strike-slip fault earthquakes for the catalog considered are shown in Figures 3a, 4a, and 5. The potency density of strike-slip fault earthquakes varies from 20 to 500 microstrain, the smallest value being associated with the 2013 Mw=6.6 Cook Strait, New Zealand earthquake (Hamling et al., 2014), presumably biased due to the depth and offshore location of the slip patch. The largest potency density is found for the 2011 Mw=6.3 Christchurch, New Zealand, the 2011 Mw=7.1 Van, Turkey, and the 2019 Mw=7.1 Ridgecrest earthquakes, illustrating the independence with earthquake magnitude. The 1992 Mw=7.3 Landers, the 1999 Mw=7.1 Hector Mine, and the 2018 Mw=7.7 Kaikoura earthquakes have a similar potency density of $\sim$ 260 microstrain, despite their different centroid depths of 4, 5, and 16 km depth, respectively. Overall we find that strike-slip fault earthquakes have the largest potency density among all events in the catalog, with no systematic trend among source characteristics, except for an increase in rupture width with centroid depth.

We now turn our attention to the source characteristics of thrust fault and megathrust earthquakes (Figures 3b, 4b, and 5). The potency density of continental thrust earthquakes ranges from

40 to 200 microstrain with centroid depths ranging from 3 to 20 km. Megathrust earthquakes span a larger depth range, from 2 to 40 km, with a range of potency density from 10 to 160 microstrain. While the distributions show some overlap, the mean potency density of continental earthquakes is therefore overall higher than their subduction zone counterparts. This is exemplified by the 2009 Mw=6.9 Qaidam (Elliott et al., 2013) and the 2015 Mw=7.9 Nepal (S. Wei et al., 2015) earthquakes. Overall, subduction zone great and giant earthquakes have the smallest potency density of all types of earthquakes considered. Potency density does not exhibit any relationship with event size when all events are considered. However, subduction zone earthquakes reach higher moment magnitudes than continental earthquakes (Figure 4). This may reflect a reduced structural complexity on subduction megathrusts that allows deep seismogenic zone earthquakes to propagate farther in the trench-parallel direction.

Among continental thrust earthquakes, there is no systematic variation of potency density with magnitude or with centroid depth. For megathrust earthquakes, however, ruptures with shallow centroid depths show a higher potency density than deeper ruptures, as the three most shallow events also have the largest potency density. This relationship is controlled by the 2010 Mw=7.7 Mentawai tsunami earthquake and the 2011 Mw=9.1 Tohoku-Oki tsunamigenic earthquake, that both have a shallow centroid depth and a high potency density. Since continental thrust earthquakes and shallow megathrust earthquakes have a higher potency density, an overall dependence of potency density with centroid depth emerges among combined thrust and megathrust earthquakes.

The potency density of slow-slip events at any depth, ranging from 0.01 to 3 microstrain, is lower than for any earthquake in the catalog, by about 2 to 3 orders of magnitudes, despite comparable potency and moment magnitude. Deep slow-slip ruptures also spread across the widest depth range of all events considered (Figure 5). Slow-slip events therefore represent an end-member of rupture style with particularly low slip efficiency distributed over a large rupture area. No discernible trend can be observed between potency and centroid depth for slow-slip events from Costa Rica (Dixon et al., 2014), Guerrero, Mexico (Radiguet et al., 2012; Bekaert et al., 2015), Hikurangi, New Zealand (Wallace & Eberhart-Phillips, 2013), and Cascadia, Pacific Northwest (Schmidt & Gao, 2010; Goodner, 2014). However, like it seems to apply to all types of events, the depth extent of slow-slip ruptures increases with their centroid depth.

4 Discussion

Our analysis reveals that potency density is independent of rupture size, considering ruptures of the same type and tectonic setting, consistent with seismological studies of stress drop (Kanamori & Anderson, 1975; Venkataraman & Kanamori, 2004; Allmann & Shearer, 2009; Ye et al., 2016b; Miyakoshi et al., 2019). The independence of potency density with size for ruptures of any type is compatible with the idea that stress drop or potency density is a fundamental properties of ruptures leading to self-similarity of the earthquake phenomenon (Cocco et al., 2016). Vallée (2013) shows that global earthquakes from the surface to 600 km depth are compatible with a constant strain drop model, although his data for events shallower than 50 km show significant scatter. Analysis of shallow earthquakes based on the same technique (Courboulex et al., 2016) shows no particular trend between stress drop and magnitude, but the changes with depth or tectonic setting are not discussed.

Our analysis shows systematic differences of potency density among types of ruptures and tectonic settings. Continental strike-slip fault earthquakes on average have the largest potency density, between 20 and 500 microstrain. Continental thrust faults earthquakes have the second highest potency density, between 40 and 200 microstrain. Shallow subduction zone ruptures, including tsunami earthquakes, are characterized with large potency density, between 100 and 200 microstrain. Deep megathrust earthquakes form a group of the lowest overall potency density, between 10 and 100 microstrain. Finally, slow-slip event form a category of their own, with a potency density between 0.01 and 3 microstrain.

The 2010 Mw=7.7 Mentawai tsunami earthquake exhibits a particularly high potency density compared to other megathrust earthquakes, including the tsunamigenic 2008 Mw=7.2 North Pagai earthquake (Salman et al., 2017). The large potency density of tsunami earthquakes may indicate the activation of strong-weakening mechanisms for near-trench ruptures, such as thermal pressurization of the frictional interface proposed by Mitsui et al. (2012) and Noda and Lapusta (2013). The simultaneous high potency density and low stress drop of tsunami earthquakes are compatible due to the low rigidity of surrounding rocks in the accretionary prism (Sallarès & Ranero, 2019).

Deep megathrust earthquakes exhibit a lower potency density and a larger rupture width than any other earthquake category. It is possible that the deep ruptures propagate into nominally slow-

slip or velocity-strengthening regions, reducing their average potency density in the process. This may explain why no periodic slow-slip has been found at subduction zones where a deep rupture recently took place, such as at the Japan trench or the Sunda trench, as the exceedingly large stress reduction caused by a large rupture may have interrupted the slow-slip cycle for a few decades (L. Feng et al., 2015; Shi et al., 2020). The low potency density of deep megathrust ruptures may also be caused by their proximity to the stability transition, which may manifest itself by a gradual reduction of coseismic weakening with increasing temperature before stable-weakening or firmly velocity-strengthening properties are attained at greater depths.

The tendency of ruptures to increase width with increasing centroid depth is clear within the catalog (Figure 5), particularly as rupture width does not scale with seismic potency (Figure 7). However, this trend may be biased in part by the upper bound of rupture width from the free surface. Indeed, by construction, the effective width cannot exceed twice the centroid depth. It is also likely that considering more events of smaller magnitude may fill the lower right quadrant of Figure 5. Ruptures on different types of faults follow a different scaling with centroid depth. Continental strike-slip events follow $w = 10^{0.43}\,\bar{z}^{0.561}$; continental thrust earthquakes $w = 10^{0.4}\,\bar{z}^{0.527}$; shallow megathrust events $w = 10^{0.03}\,\bar{z}^{0.93}$; and other megathrust events $w = 10^{0.12}\,\bar{z}^{0.86}$. The sub-linear relationship between width and centroid depth in log-log space for all events, with a power exponent of 0.76, indicates the tendency of most earthquakes to not break the surface, or to exhibit less slip near the surface, broadly compatible with the concept of shallow slip deficit (Fialko et al., 2005).

The deep slow-slip events, which represent the widest ruptures of the catalog despite their small magnitude, scatter along the same trend as other type of events across various tectonic contexts. Since the source mechanism of slow and fast earthquakes may be widely different, this result indicates that similar scaling of source properties can be obtained for different events, but for different reasons. For example, Cattania and Segall (2018) discuss how the relationships among magnitude, duration, and stress drop can be similar in numerical simulations of seismic cycles, but for different underlying reasons. Slow-slip events have been found to follow the same moment-duration scaling as fast ruptures (Michel et al., 2019), despite their widely different radiation efficiency.

The large variations of potency density across tectonic settings and depth can be due to the activation of different rupture processes. For instance, the high potency density observed for continental subduction zone earthquakes and tsunami earthquakes may be attributed to strong weakening mechanisms such as flash weakening (Hirose & Bystricky, 2007; N. M. Beeler et al., 2008; Kitajima et al., 2011; Goldsby & Tullis, 2011) and thermal pressurization (Andrews, 2002; Hirose & Bystricky, 2007; Mitsui et al., 2012; Noda & Lapusta, 2013; Viesca & Garagash, 2015). The potency density of such events may be approximated with

$$\epsilon \propto \frac{\Delta\mu\,\bar{\sigma}}{2G} \ , \tag{9}$$

where $0.1 \lesssim \Delta\mu \lesssim 0.6$ represents a large drop of frictional strength (e.g., Toro et al., 2004, 2006) and $60 \lesssim \bar{\sigma} \lesssim 100\,\mathrm{MPa}$ is the effective normal stress, leading to potency density of the order of 100 to 500 microstrain. Hence, ruptures with potency density larger than about 100 microstrain may be associated with strong weakening. This would imply that most continental strike-slip fault and continental thrust ruptures operate under this condition, compatible with the claims of Viesca and Garagash (2015). Smaller potency densities may be explained in the framework of rate-and-state friction (Dieterich, 1979; Ruina, 1983; Barbot, 2019a) following

$$\epsilon \propto \frac{(b-a)\bar{\sigma}}{2G} \ , \tag{10}$$

where $(b-a) \sim 4\times10^{-3}$ is the steady-state parameters controlling the velocity dependence of friction (Scholz, 1998; Lapusta & Barbot, 2012), or simply $1 \lesssim (b-a)\bar{\sigma} \lesssim 10\,\mathrm{MPa}$, leading to a potency density in the range of 15 to 150 microstrain. However, this estimate may vary greatly because of dynamic stress overshoot or undershoot (Kanamori & Rivera, 2006) and the detailed geometry of a rupture. Slow-slip events occur in the stable weakening regime, corresponding to failed nucleations (Liu & Rice, 2005, 2007; Segall et al., 2010; Goswami & Barbot, 2018; Bürgmann, 2018; Barbot, 2019b). Hence, their total slip scales with the characteristic weakening distance, as in

$$\epsilon \propto \frac{L}{R} \ , \tag{11}$$

where $1 \lesssim L \lesssim 10\,\mathrm{cm}$ is the characteristic weakening distance of rate-and-state friction in a range compatible with slow slip and $R \sim 50\,\mathrm{km}$ is the down-dip rupture width, leading to estimates of potency density in the range of 0.01 to 3 microstrain. The overall variability of source properties, e.g., two orders of magnitude for potency density, may be attributed to the presence of frictional contrast along the fault (Kaneko et al., 2010; Kaneko & Shearer, 2015), variability of earthquake slip due to the stress shadow of previous ruptures (Michel et al., 2017; Barbot, 2019b), morphological gradients (Qiu et al., 2016; Sathiakumar et al., 2019), variation of off-fault damage (Cappa et al., 2014), differing coupling coefficients (Chounet & Vallée, 2018), or the activation of different weakening mechanisms (Kirkpatrick & Shipton, 2009; Cocco et al., 2016; Cattania & Segall, 2018).

The variability of potency density among events has important implications on the moment-duration scaling relationship of slow-slip events, which may differ from that of fast ruptures (Peng & Gomberg, 2010). Simple models provide a rationale to understand the moment-duration scaling of slow and fast ruptures. For slow-slip events, we may assume that the rupture spreads rapidly across a fixed down-dip width W and then propagates along strike for most of the duration of the event at a constant rupture velocity between 0.01 and 0.1 m/s. This leads to the along-strike rupture length $L = V_r T$ and the rupture area $A = W V_r T$, where V_r is the rupture velocity and T is the rupture duration. The relationship between slip and potency density $s \approx \epsilon\, W$ also holds. The moment released by slow-slip events can then be defined as

$$M \approx G W V_r \epsilon\, T \ , \tag{12}$$

showing a linear relationship among moment, duration, and potency density. For fast ruptures, a simple model assumes a linear relationship between rupture duration and rupture radius, leading to

$$M \approx G V_r^3 \epsilon\, T^3 \ , \tag{13}$$

which shows a power law between moment and duration. More sophisticated models of fast ruptures that incorporate the propagation of aseismic slip into the rupture area provide slightly different power exponents (Chen & Lapusta, 2009; Cattania & Segall, 2018). Deciphering the moment-duration scaling for slow-slip events is important to better understand the underlying source processes. However,

large variations of potency density of about two orders of magnitude (Figures 3 and 4) can introduce important bias if potency density is not included in the analysis. This may explain the contradictory results found at the Cascadia subduction zone, where Gao et al. (2012) and Michel et al. (2019) found linear and cubic moment-duration scalings, respectively, for events rupturing similar sections of the Cascadia megathrust. To shed more light on this problem, we investigate the relationship among moment, duration, and potency density with the catalog of slow-slip events. For the collection of slow-slip events considered, the duration ranges between 7 days and 180 days, the moment covers two orders of magnitude, between 5×10^{18} to 5×10^{20} Nm, and the potency density varies between 0.01 and 3 microstrains, providing a sufficient dynamic range to investigate the scaling relationships. Event duration increases with potency density, with $T \approx \epsilon^{0.2}$ for the entire catalog (Figure 8). The largest outlier corresponds to a near-trench event at the Hikurangi subduction zone that may involve a different rupture mechanism than its deep counterparts. The moment-duration relationship (Figure 9) shows large variability that cannot be reduced by either the linear and cubic root scaling laws, whether or not regions are considered individually or together. We conclude that variations in potency density among slow-slip events preclude a simple characterization in terms of a linear or cubic root scaling between moment and duration. Several micro-physical mechanisms of deformation may be responsible for the slow-slip phenomenon, including stable weakening (Liu & Rice, 2005, 2007; Veedu & Barbot, 2016), dilatant hardening (Segall et al., 2010), semi-brittle deformation (Goswami & Barbot, 2018), fluid pulses (Cruz-Atienza et al., 2018), and possibly thermal instabilities. In addition, some slow-slip events do not occur spontaneously, but are triggered by distant seismic events (Zigone et al., 2012). It is possible that a single scaling relationship may be inadequate to capture a such wide range of rupture mechanisms. In addition, a constant rupture velocity may not be applicable during nucleation, propagation, and arrest of slow-slip ruptures.

5 Conclusion

We gather a catalog of slow and fast earthquake slip distributions derived from the analysis of geodetic and other geophysical data to better understand the static source properties of continental and subduction earthquakes and slow-slip events. We estimate simple source characteristics, such as centroid depth, width, potency, and potency density, with limited bias from unknown variability of

elastic properties. This allows us to compare events of different styles from various tectonic settings and source depths. The potency density, a fundamental property of ruptures related to stress drop affecting rupture size and rupture style, varies significantly depending on the tectonic setting and, in the case of megathrust earthquakes, centroid depth. In particular, the potency density of shallow earthquakes and tsunami earthquakes is higher than their deep counterpart. This implies systematic variation of rupture processes with depth on a megathrust, with strong weakening being more prominent closer to the trench. Deep megathrust earthquake share a lower potency density, indicative of less efficient weakening mechanisms or the propagation of deep ruptures into stable-weakening regions. Slow-slip events at subduction zones represent an end-member of large ruptures characterized with low potency density. Large variability in potency density among slip-slip events, which affects duration, makes simple scaling relationships for the moment-duration scaling inadequate. If large potency density is indicative of strong weakening mechanisms, most continental strike-slip fault and continental thrust ruptures operate under this condition.

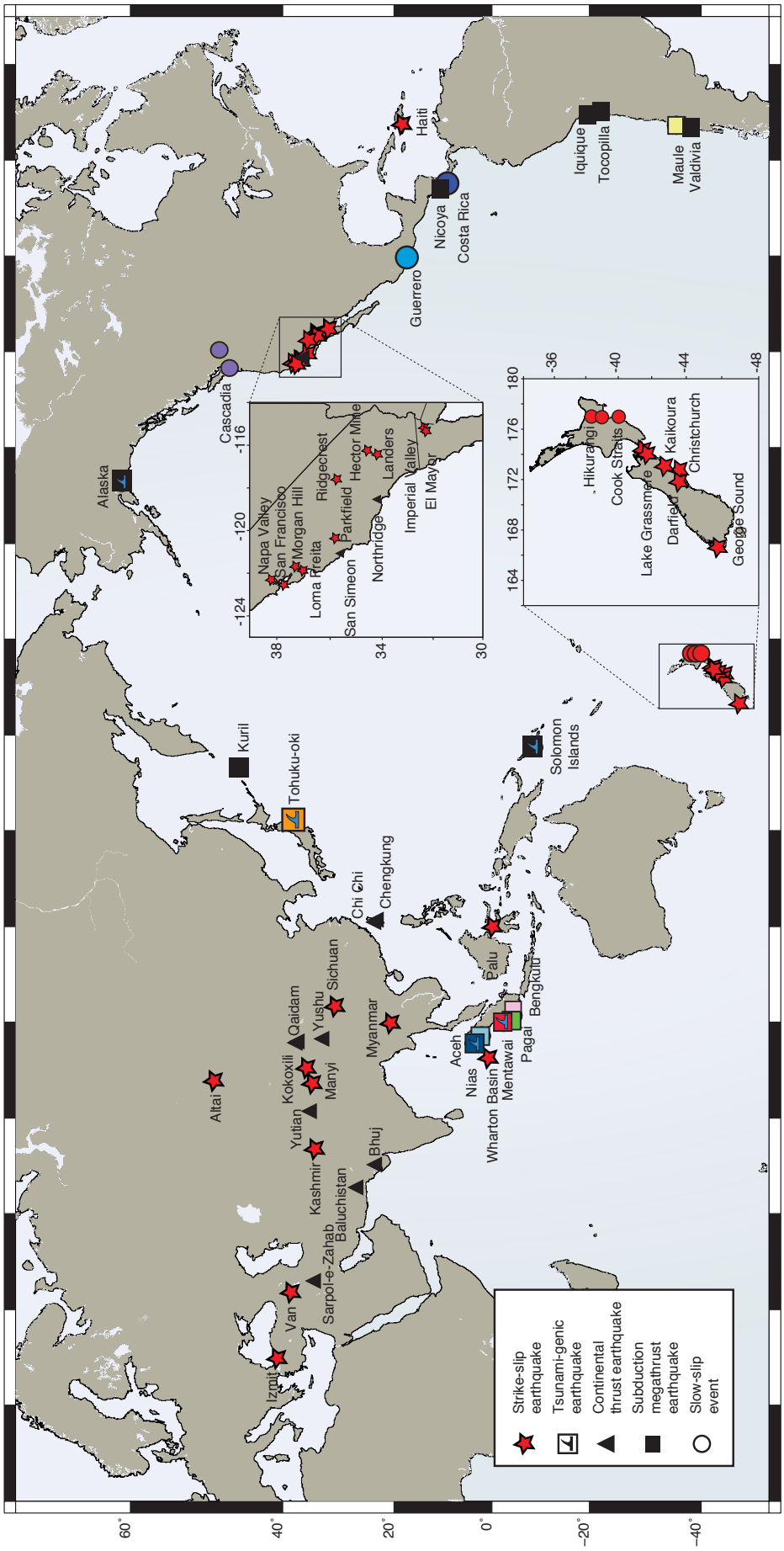

Figure 1. The distribution of slow and fast earthquakes considered in this study. The catalog includes thrust fault and megathrust earthquakes (25 events), strike-slip fault earthquakes (red stars, 27 events), and slow-slip events on subduction megathrusts (circles, 17 events), adding to 65 events. The squares represent megathrust events; the color is for rapid identification in subsequent figures. The triangles show continental thrust earthquakes.

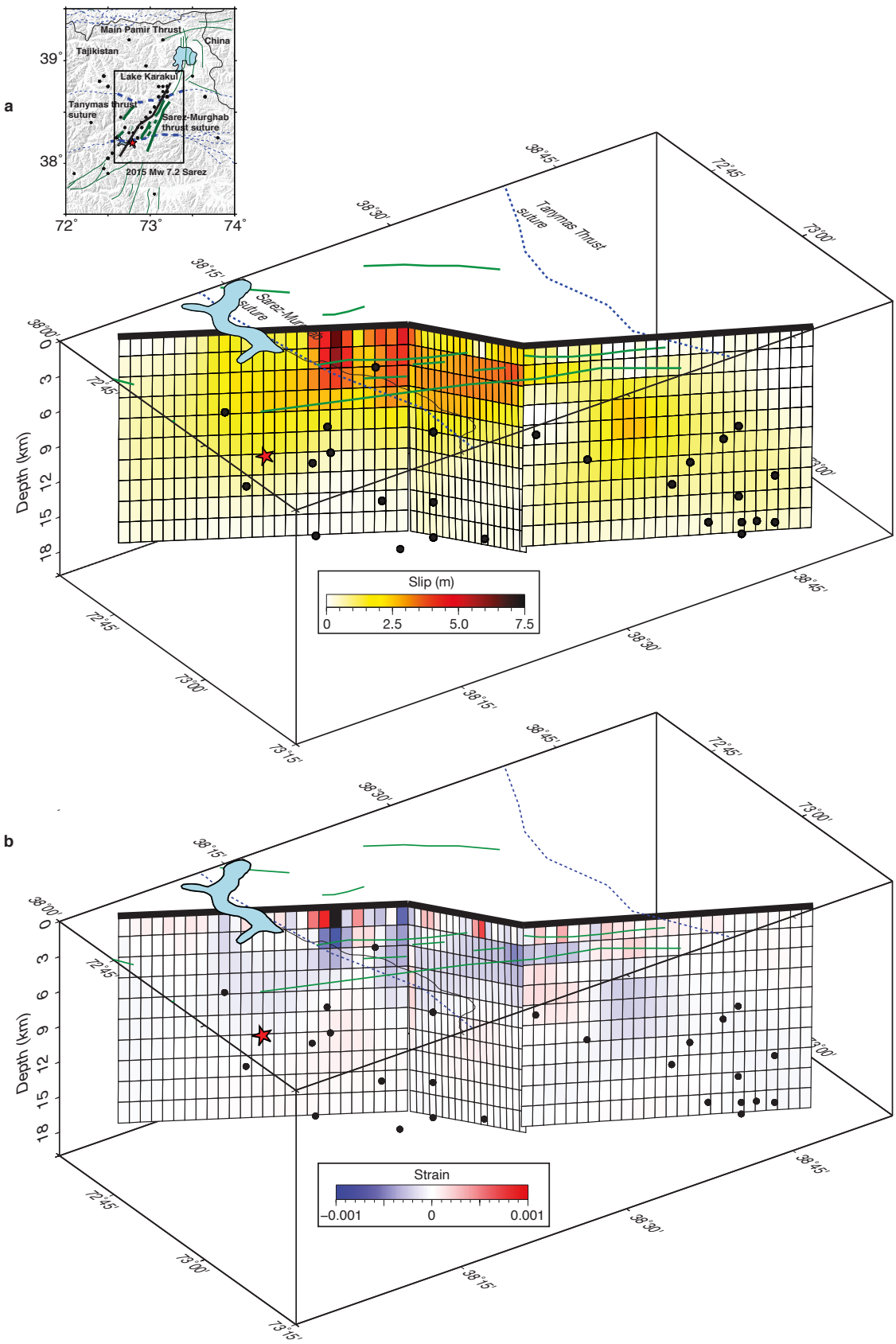

Figure 2. Slip and strain distribution for the 2015 Mw 7.2 Lake Sarez, Tajikistan earthquake. a) Slip distribution inferred from SAR and InSAR data. The star marks the hypocenter. b) Distribution of strain along the fault. When averaged over the entire slip region and weighted by slip, the potency density of the earthquake is estimated at 96.1 microstrain.

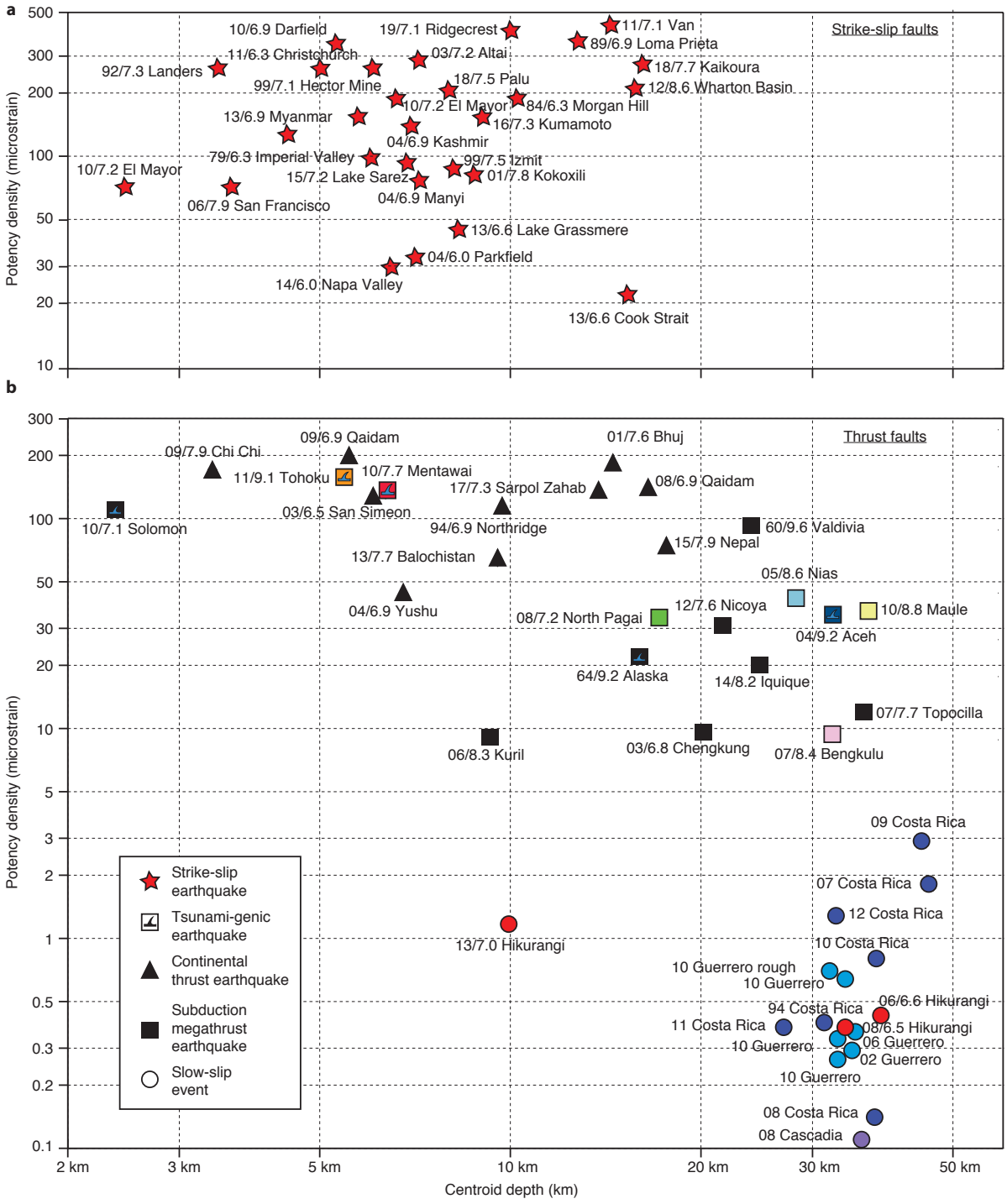

Figure 3. Variation of potency density with centroid depth of all events in the catalog. a) Distribution of potency density with centroid depth for strike-slip earthquakes. b) Potency density of thrust faults and megathrust events. Shallow events, predominantly strike-slip or tsunami earthquakes, are characterized with large potency density. Deep megathrust earthquakes tend to have a lower potency density. Deep slow-slip events, with with potency densities orders of magnitude smaller than strike-slip fault earthquakes, form an end-member of rupture style.

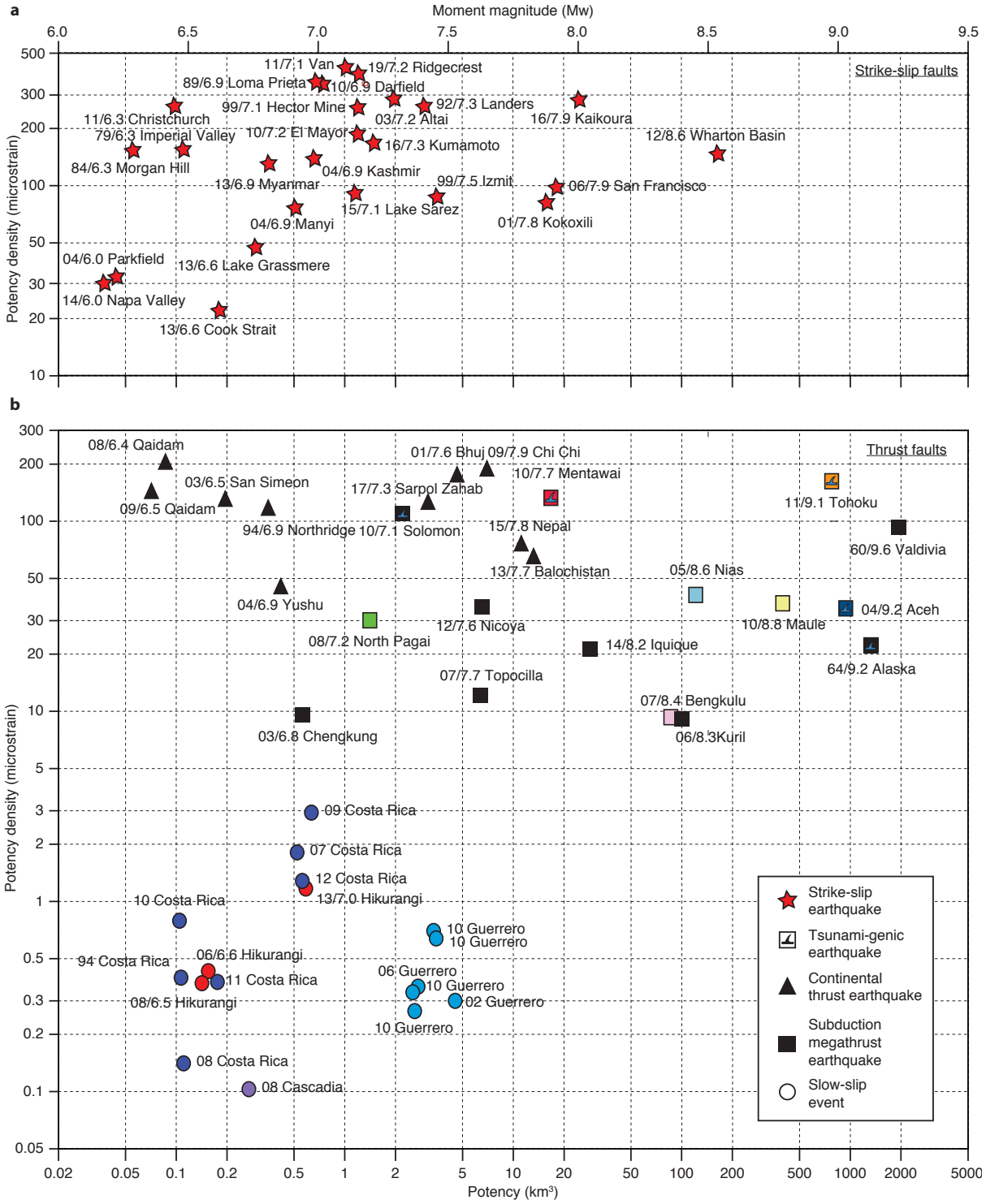

Figure 4. Variation of potency density with rupture size. a) Strike-slip fault earthquakes. b) Thrust fault and megathrust events. There is no systematic variation of potency density and potency and moment magnitude (computed assuming a uniform rigidity of 30 GPa). Slow-slip events have potency densities lower than for any type of earthquake.

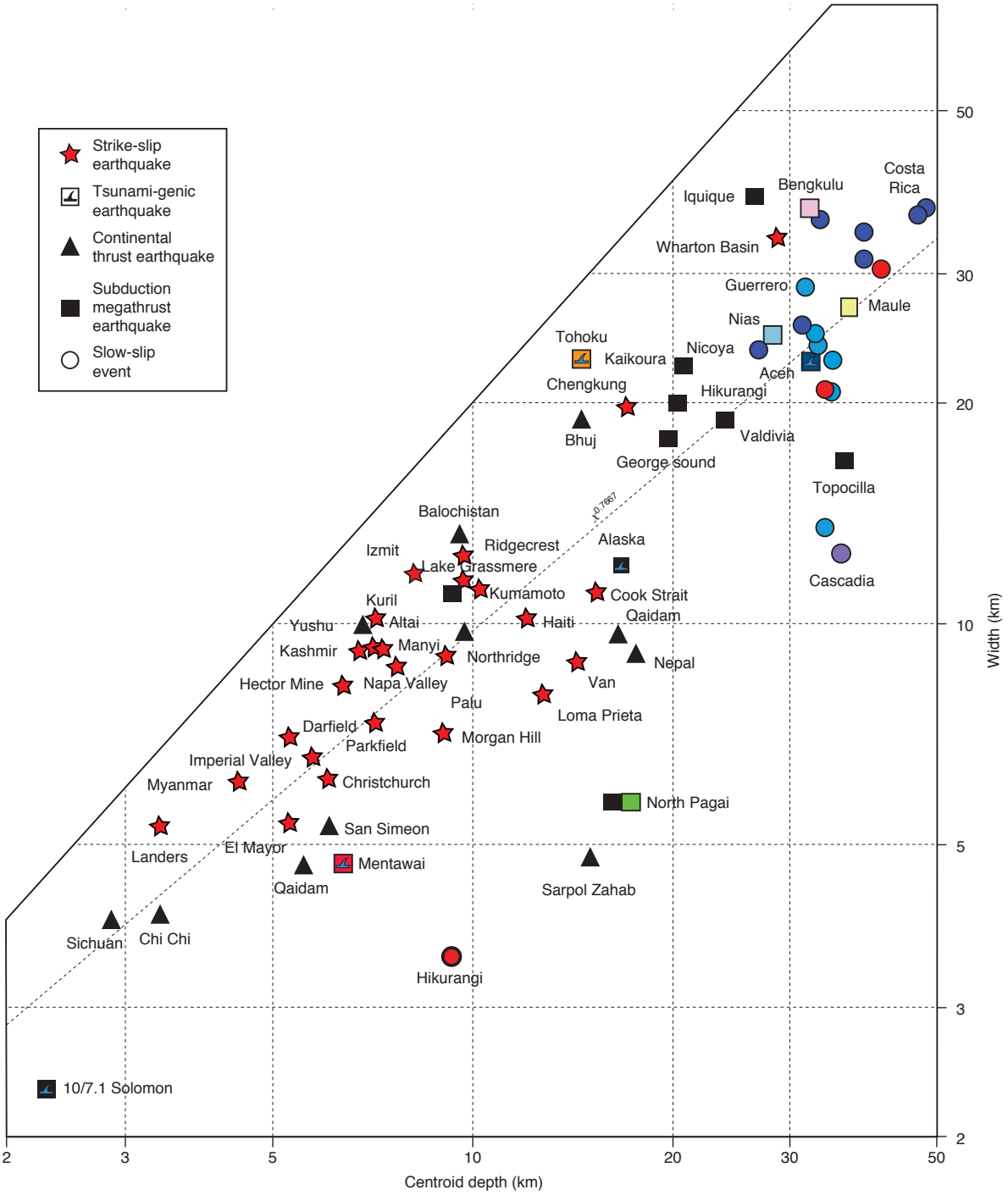

Figure 5. Variation of rupture width with centroid depth, illuminating a apparent relationship between the depth extent of ruptures and their respective slip-averaged centroid depth. The shallowest events are continental earthquakes and tsunami earthquakes, which are also the events with the smallest down-dip extent. Megathrust earthquake occupy a greater depth range than continental earthquakes. Deep megathrust slow slip event span the largest width of all event types, following a similar trend as any other type of event. The overall width/depth relationship for all events follows a power-law with a power exponent of 0.76. The exponent varies for different type of events, as discussed in the main text.

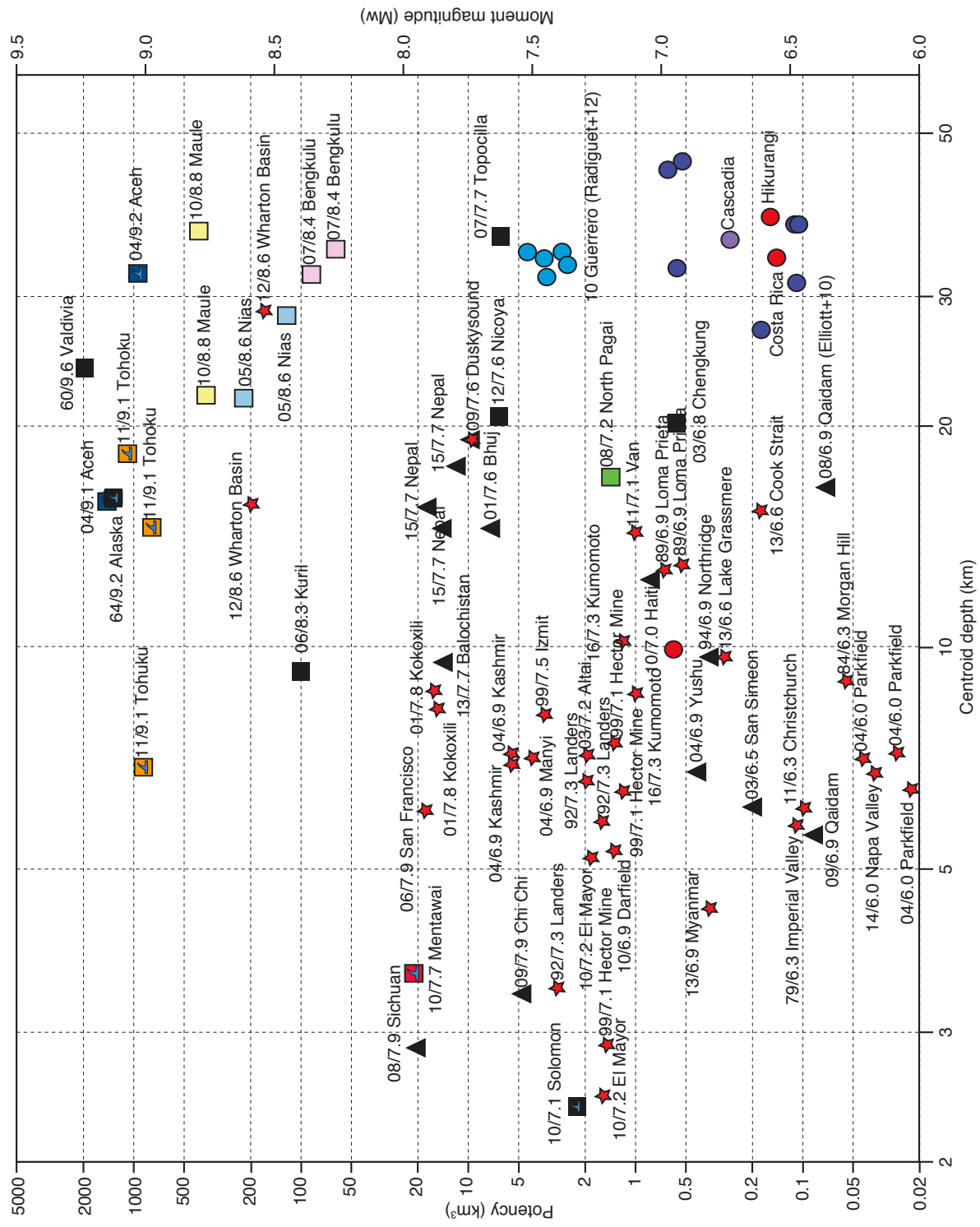

Figure 6. Variation of potency with centroid depth for all events in the catalog. Moment magnitude is computed using a uniform rigidity of 30 GPa. There is no apparent relationship between potency and centroid depth, considering events within similar tectonic settings or rupture styles.

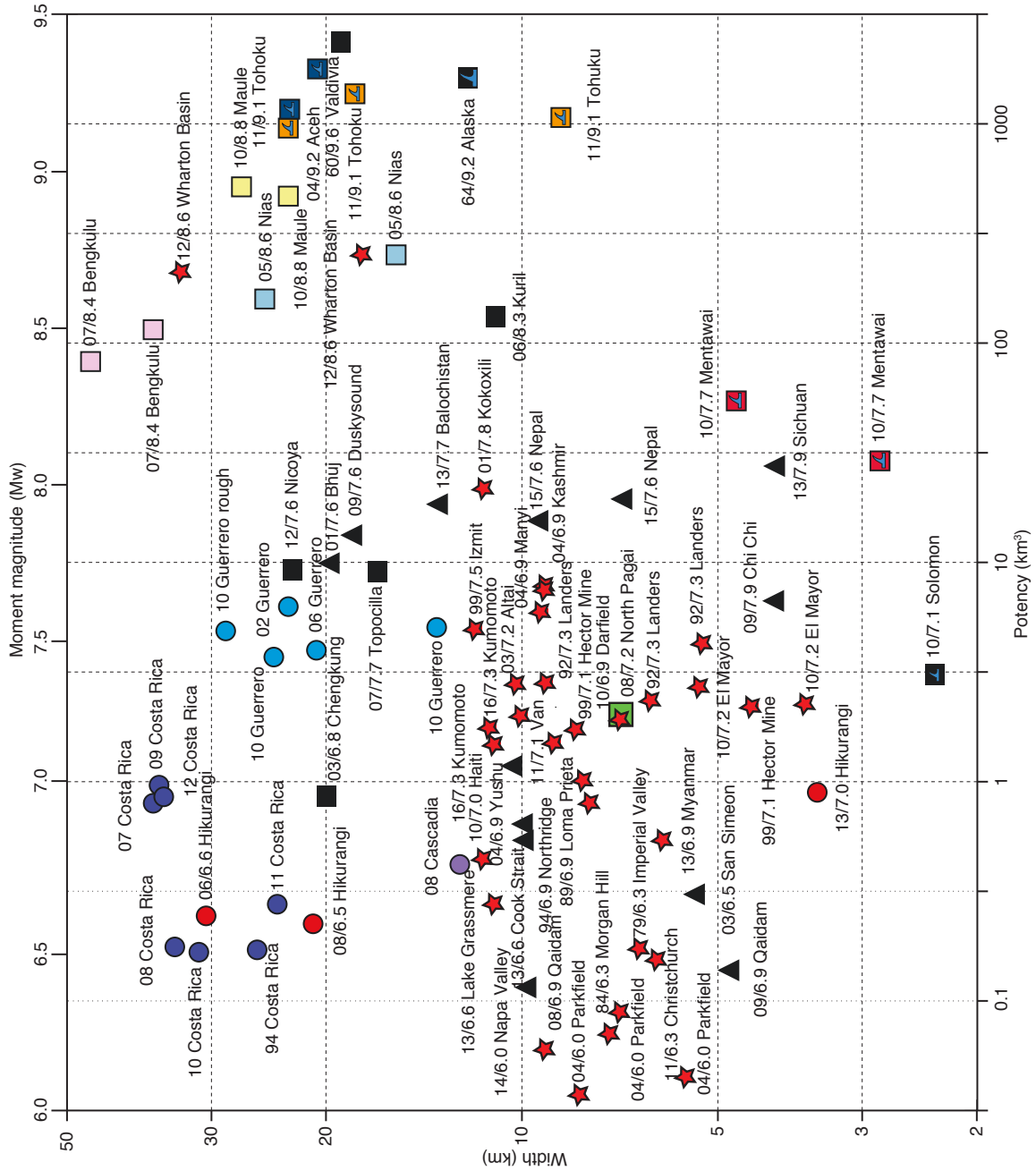

Figure 7. Variation of potency with width in the depth direction for all events in the catalog. Rupture size, i.e., potency or moment magnitude, does not seem to control rupture width, even considering events of similar tectonic setting or rupture style.

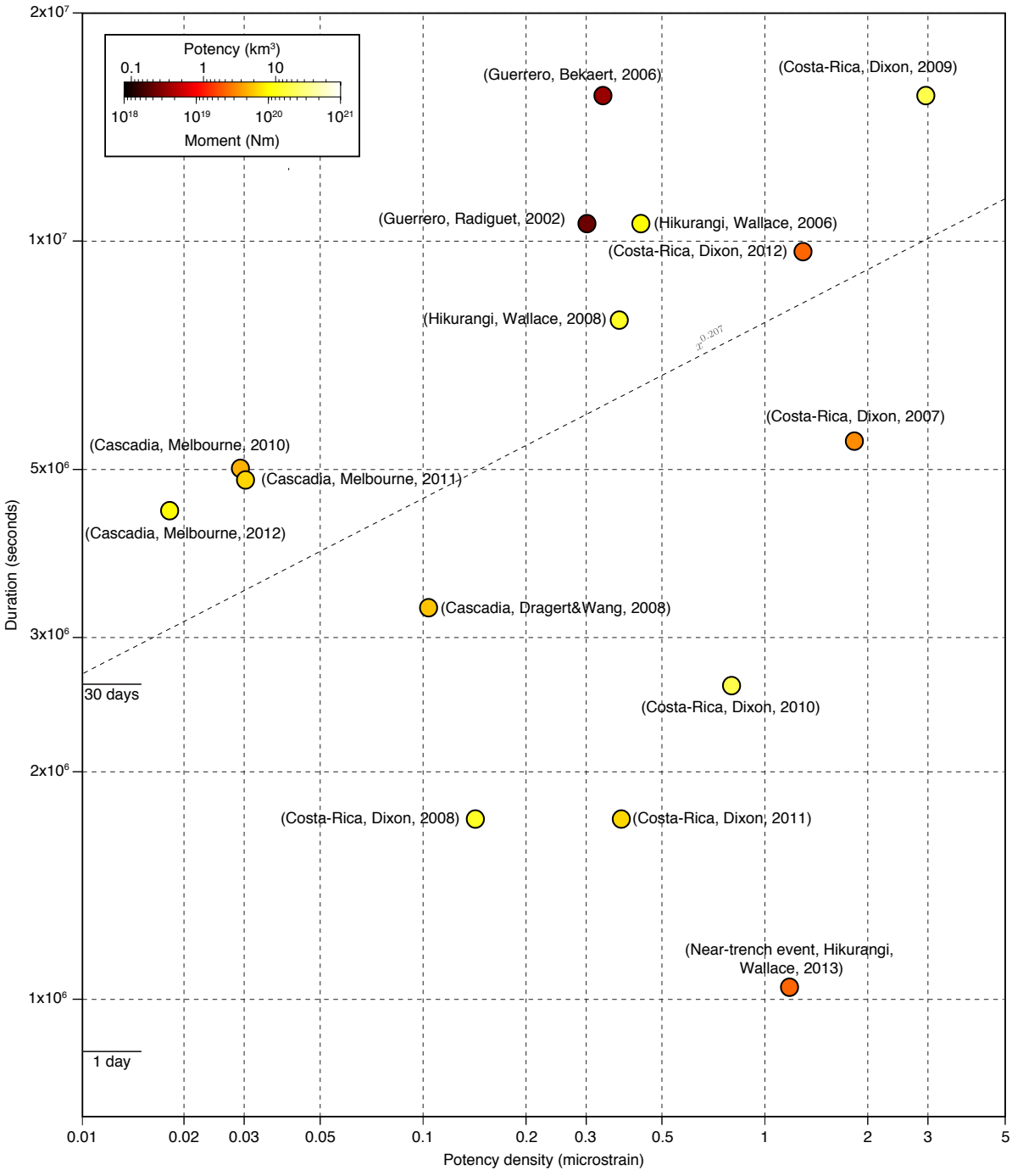

Figure 8. Variation of potency density with event duration for all the slow-slip events in the catalog. The duration of events scales sublinearly with potency density as $x^{0.276}$. The 2013 Hikurangi event is an outlier, presumably due to its shallow centroid depth, pointing to a different rupture mechanism than for deeper events.

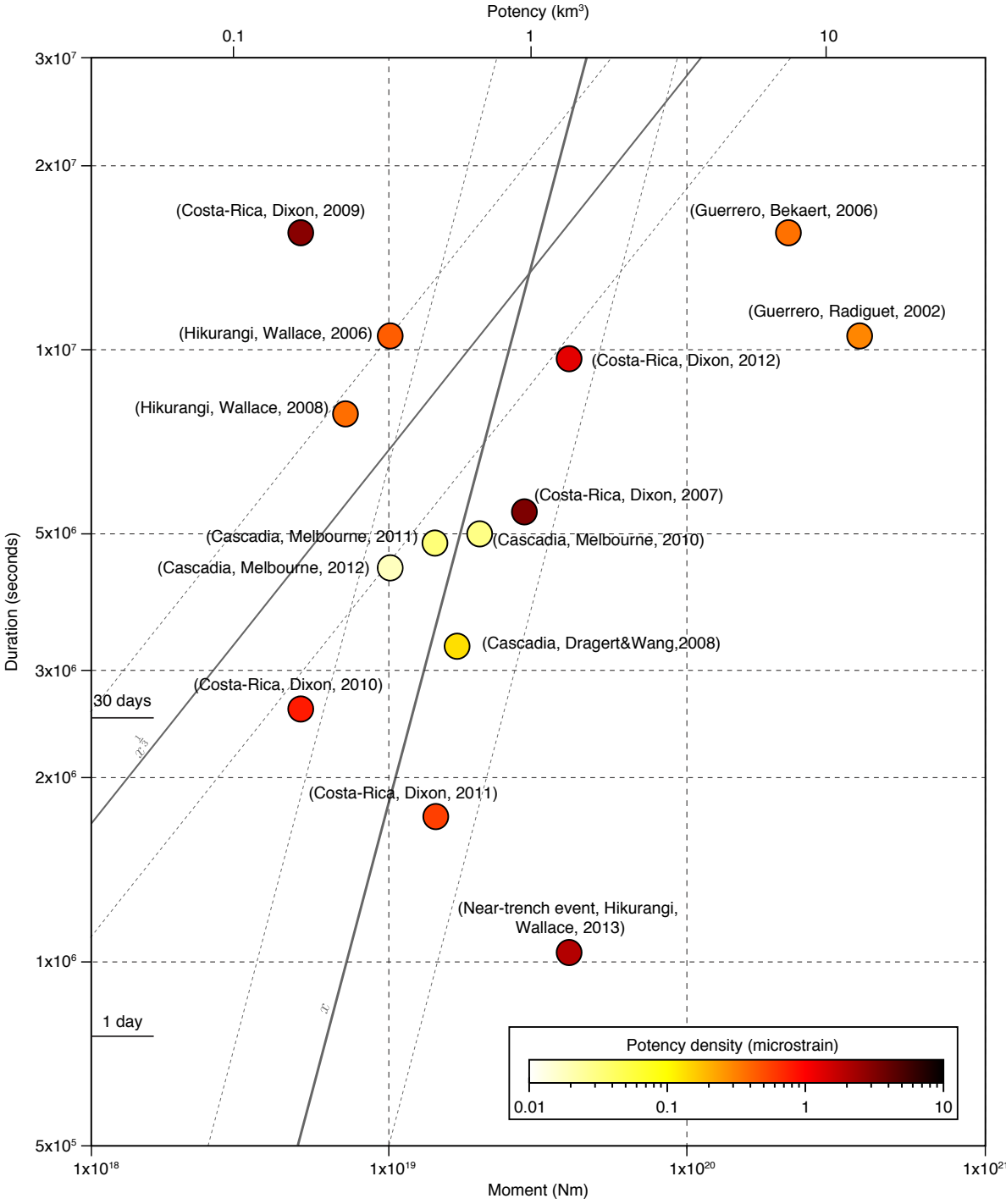

Figure 9. Variation of moment with event duration for all the slow-slip events in the catalog. All the events appear to neither favor the $M \propto T$ nor the $M \propto T^3$ scaling law, whether considering individual regions or all the events together.

Table 1. Slip distribution and source characteristics of 27 strike-slip fault earthquakes from magnitude Mw=6.0 to 8.6 considering 35 different models.

Name	Country	Year	Mw	Potency density	Centroid depth	Width (km)	Reference
Altai	Russia	2003	7.2	287.9	7.1	10.2	Barbot et al. (2008b)
Balochistan	Pakistan	2013	7.7	63.2	9.5	13.2	Avouac et al. (2014)
Bam	Iran	2003	6.6	82.28	2.6	4.157	Fialko et al. (2005)
Christchurch	New Zealand	2011	6.3	263.7	6.0	6.2	Elliott et al. (2012)
Cook Straits	New Zealand	2013	6.6	22.1	15.3	11.0	Hamling et al. (2014)
Darfield	New Zealand	2010	6.9	344.7	5.3	7.0	Elliott et al. (2012)
El Mayor	Mexico	2010	7.2	71.6	5.2	5.2	S. Wei et al. (2013)
Haiti	Haiti	2010	7.0	130.8	12.4	12.4	Symithe et al. (2013)
Hector Mine	USA	1999	7.1	259.1	6.4	8.2	Salichon et al. (2004)
Imperial Valley	USA	1979	6.3	154.7	5.7	5.7	Zeng and Anderson (2000)
Izmit	Turkey	1999	7.6	87.6	8.1	11.7	Toksoz et al. (1999)
Kaikoura	New Zealand	2016	7.9	325.7	15.8	19.0	T. Wang, Wei, et al. (2018)
Kokoxili	China	2001	7.9	81.8	8.7	11.4	Lasserre et al. (2005)
Kumomoto	Japan	2016	7.3	188.3	10.2	11.1	Moore et al. (2017)
Landers	USA	1992	7.3	263.5	3.4	5.3	Fialko (2004)
Lake Grassmere	New Zealand	2013	6.6	47.0	9.7	11.5	Hamling et al. (2014)
Lake Sarez	Tajikistan	2015	7.2	96.1	6.5	9.1	Nanjundiah, pers. comm.
Loma Prieta	USA	1989	6.9	354.7	12.7	8.0	Zeng and Anderson (2000)
Manyi	China	2004	7.6	76.7	7.1	9.3	H. Wang et al. (2007)
Morgan Hill	USA	1984	6.3	154.0	9.0	7.1	Beroza and Spudich (1988)
Myanmar	Myanmar	2011	6.9	127.0	4.4	6.1	Y. Wang et al. (2014)
Napa Valley	USA	2014	6.0	30.7	6.7	9.2	S. Wei et al. (2014)
Palu	Sarawak	2018	7.5	204.8	7.3	8.14	S. Wei, pers. Comm.
Parkfield	USA	2004	6.0	33.1	7.1	7.4	Barbot et al. (2012)
Ridgecrest	California	2019	7.1	407.3	9.9	12.6	S. Wei, pers. Comm.
San Francisco	USA	1906	7.9	98.5	6.0	6.0	Song et al. (2008)
Van	Turkey	2011	7.1	422.2	14.3	8.9	Elliott et al. (2013)
Wharton Basin	Sumatra	2012	8.6	211.1	15.7	33.4	Hill et al. (2015)

Table 2. Slip distributions and source characteristics of 25 thrust and megathrust earthquakes considering 34 different models.

Name	Country	Year	Mw	Potency density	Centroid depth (km)	Width	Reference
Aceh	Sumatra	2004	9.2	34.9	32.2	22.75	Chlieh et al. (2007)
Alaska	USA	1964	9.2	22.0	16.0	12.0	Johnson et al. (1996)
Bengkulu	Sumatra	2007	8.4	9.4	32.13	36.8	Tsang et al. (2016)
Bhuj	India	2001	7.6	182.7	14.5	19.1	Copley et al. (2011)
Chengkung	Taiwan	2003	6.8	9.6	20.2	20	Thomas et al. (2014)
Chi-Chi	Taiwan	1999	7.5	170.7	3.4	4.01	Yu et al. (2001)
Gorkha	Nepal	2015	7.8	22.2	14.5	9.2	S. Wei et al. (2018)
Iquique	Chile	2014	8.2	20.5	25.5	39.0	Gusman et al. (2015)
Kashmir	Kashmir	2005	7.6	118.4	7.2	9.15	Avouac et al. (2006)
Kuril	Alaska	2006-07	8.3	9.1	9.3	11	Steblov et al. (2008)
Maule	Chile	2010	8.8	36.3	36.8	22.8	Luttrell et al. (2011)
Mentawai	Sumatra	2010	7.8	132.7	6.3	4.7	Yue, Lay, Rivera, Bai, et al. (2014)
Nias	Sumatra	2005	8.6	40.9	28.3	15.6	Konca et al. (2007)
Nicoya	Costa Rica	2012	7.6	35.5	20.6	22.5	Yue et al. (2013)
Northridge	USA	1994	6.9	113.6	9.7	9.8	Hudnut et al. (1996)
Pagai	Sumatra	2008	7.2	35.5	17.2	5.4	Salman et al. (2017)
Qaidam	China	2008	6.3	139.2	16.5	9.6	Elliott et al. (2011)
Qaidam	China	2009	6.3	198.5	5.6	4.7	Elliott et al. (2011)
San Simeon	USA	2003	6.5	126.7	6.1	5.3	Ji et al. (2004)
Sarpol Zahab	Iran	2017	7.3	128.9	14.6	4.8	W. Feng et al. (2018)
Solomon Isl.	Solomon Isl.	2010	7.1	110.0	2.4	2.3	Newman, Feng, et al. (2011)
Tohoku-Oki	Japan	2011	9.1	160.8	6.9	17.7	Bletery et al. (2014)
Topocilla	Chile	2007	7.7	12.0	36.1	16.6	Bejar Pizarro et al. (2010)
Valdivia	Chile	1960	9.6	93.7	24.0	19.0	Moreno et al. (2009)
Yushu	China	2010	6.9	43.9	6.8	9.9	Li et al. (2011)

Table 3. Slip distributions and source characteristics of 17 slow-slip events on subduction megathrusts used in the study.

Name	Country	Year	Mw	Potency density	Centroid depth (km)	Width	Reference
Cascadia	USA	2008	6.75	0.103	35.8	12.5	Dragert and Wang (2011)
Cascadia	USA	2010	6.84	0.029	36.4	29.92	Goodner (2014)
Cascadia	USA	2011	6.77	0.030	36.61	32.32	Goodner (2014)
Cascadia	USA	2012	6.83	0.018	35.86	36.25	Goodner (2014)
Cascadia	USA	2013	6.85	0.035	38.19	34.08	Goodner (2014)
Costa Rica	Costa Rica	2007	6.92	1.80	45.8	36.9	Dixon et al. (2014)
Costa Rica	Costa Rica	2008	6.48	0.14	37.6	34.1	Dixon et al. (2014)
Costa Rica	Costa Rica	2009	6.97	2.93	44.6	36.0	Dixon et al. (2014)
Costa Rica	Costa Rica	2010	6.46	0.79	37.6	31.4	Dixon et al. (2014)
Costa Rica	Costa Rica	2011	6.61	0.38	27.0	23.7	Dixon et al. (2014)
Costa Rica	Costa Rica	2012	6.94	1.28	32.8	35.5	Dixon et al. (2014)
Guerrero	Mexico	2002	7.5	0.30	34.5	22.9	Radiguet et al. (2012)
Guerrero	Mexico	2006	7.3	0.35	34.5	20.7	Radiguet et al. (2012)
Guerrero	Mexico	2010	7.4	0.65	33.8	13.5	Radiguet et al. (2012); Bekaert et al. (2015)
Hikurangi	New Zealand	2006	6.55	0.37	33.9	30.4	Wallace and Eberhart-Phillips (2013);
Hikurangi	New Zealand	2008	6.58	0.43	38.5	20.8	Wallace and Eberhart-Phillips (2013);
Hikurangi	New Zealand	2013	6.95	1.17	9.9	3.5	Wallace and Eberhart-Phillips (2013);

Acknowledgments

The study benefited from funding from the National Science Foundation, under award number EAR-1848192. This work comprises Earth Observatory of Singapore contribution no. 267. This research was also supported by the National Research Foundation (NRF) Singapore under its NRF Fellowship scheme (award no. NRF-NRFF2013-06) and by the Earth Observatory of Singapore (EOS) and the Singapore Ministry of Education under the Research Centres of Excellence initiative.

References

Aki, K. (1967). Scaling law of seismic spectrum. *J. Geophys. Res.*, *72*(4), 1217–1231. doi: 10.1029/JZ072i004p01217

Aki, K. (1979). Characterization of barriers on an earthquake fault. *J. Geophys. Res.*, *84*(B11), 6140–6148. doi: 10.1029/JB084iB11p06140

Allmann, B. P., & Shearer, P. M. (2009). Global variations of stress drop for moderate to large earthquakes. *J. Geophys. Res.*, *114*(B1). doi: 10.1029/2008JB005821

Amey, R., Hooper, A., & Walters, R. (2018). A bayesian method for incorporating self-similarity into earthquake slip inversions. *J. Geophys. Res.*, *123*(7), 6052–6071. doi:

10.1029/2017JB015316

Andrews, D. (2002). A fault constitutive relation accounting for thermal pressurization of pore fluid. *J. Geophys. Res.*, *107*(B12), ESE–15. doi: 10.1029/2002JB001942

Aster, R. C., Borchers, B., & Thurber, C. H. (2012). *Parameter estimation and inverse problems* (2nd ed.). Academic Press.

Atzori, S., & Antonioli, A. (2011). Optimal fault resolution in geodetic inversion of coseismic data. *Geophys. J. Int.*, *185*(1), 529-538. doi: 10.1111/j.1365-246X.2011.04955.x

Avouac, J. P., Ayoub, F., Leprince, S., Konca, O., & Helmberger, D. V. (2006). The 2005, Mw 7.6 Kashmir earthquake: Sub-pixel correlation of ASTER images and seismic waveforms analysis. *Earth Planet. Sci. Lett.*, *249*(3-4), 514–528. doi: 10.1016/j.epsl.2006.06.025

Avouac, J.-P., Ayoub, F., Wei, S., Ampuero, J.-P., Meng, L., Leprince, S., ... Helmberger, D. (2014). The 2013, Mw 7.7 Balochistan earthquake, energetic strike-slip reactivation of a thrust fault. *Earth Planet. Sci. Lett.*, *391*, 128–134. doi: 10.1016/j.epsl.2014.01.036

Avouac, J.-P., Meng, L., Wei, S., Wang, T., & Ampuero, J.-P. (2015). Lower edge of locked Main Himalayan Thrust unzipped by the 2015 Gorkha earthquake. *Nature Geosci.*. doi: 10.1038/ngeo2518

Baltay, A., & Hanks, T. C. (2014). Understanding the magnitude dependence of PGA and PGV in NGA-West 2 data. *Bull. Seism. Soc. Am.*, *104*(6), 2851–2865. doi: 10.1785/0120130283

Baltay, A., Ide, S., Prieto, G., & Beroza, G. (2011). Variability in earthquake stress drop and apparent stress. *Geophys. Res. Lett.*, *38*(6). doi: 10.1029/2011GL046698

Barbot, S. (2019a). Modulation of fault strength during the seismic cycle by grain-size evolution around contact junctions. *Tectonophysics*, *765*, 129-145. doi: 10.1016/j.tecto.2019.05.004

Barbot, S. (2019b). Slow-slip, slow earthquakes, period-two cycles, full and partial ruptures, and deterministic chaos in a single asperity fault. *Tectonophysics*, *768*, 228171. doi: 10.1016/j.tecto.2019.228171

Barbot, S., Agram, P., & De Michele, M. (2013). Change of Apparent Segmentation of the San Andreas Fault Around Parkfield from Space Geodetic Observations Across Multiple Periods. *J. Geophys. Res.*, *118*(12), 6311-6327.

Barbot, S., & Fialko, Y. (2010). A unified continuum representation of postseismic relaxation

mechanisms: semi-analytic models of afterslip, poroelastic rebound and viscoelastic flow. *Geophys. J. Int.*, *182*(3), 1124-1140. doi: 10.1111/j.1365-246X.2010.04678.x

Barbot, S., Fialko, Y., & Bock, Y. (2009). Postseismic Deformation due to the Mw 6.0 2004 Parkfield Earthquake: Stress-Driven Creep on a Fault with Spatially Variable Rate-and-State Friction Parameters. *J. Geophys. Res.*, *114*(B07405). doi: 10.1029/2008JB005748

Barbot, S., Hamiel, Y., & Fialko, Y. (2008a). Space geodetic investigation of the coseismic and postseismic deformation due to the 2003 Mw 7.2 Altai earthquake: Implications for the local lithospheric rheology. *J. Geophys. Res.*, *113*(B03403). doi: 10.1029/2007JB005063

Barbot, S., Hamiel, Y., & Fialko, Y. (2008b). Space geodetic investigation of the coseismic and postseismic deformation due to the 2003 Mw7.2 Altai earthquake: Implications for the local lithospheric rheology. *J. Geophys. Res.*, *113*(3), 1–15. doi: 10.1029/2007JB005063

Barbot, S., Lapusta, N., & Avouac, J. P. (2012). Under the hood of the earthquake machine: Toward predictive modeling of the seismic cycle. *Science*, *336*(6082), 707–710. doi: 10.1126/science.1218796

Bechor, N. B. D., & Zebker, H. A. (2006). Measuring two-dimensional movements using a single InSAR pair. *Geophys. Res. Let.*, *33*, L16311. doi: 10.1029/2006GL026883

Beeler, N., Hickman, S., & Wong, T.-f. (2001). Earthquake stress drop and laboratory-inferred interseismic strength recovery. *J. Geophys. Res.*, *106*(B12), 30701–30713. doi: 10.1029/2000JB900242

Beeler, N. M., Tullis, T. E., & Goldsby, D. L. (2008). Constitutive relationship and physical basis of fault strength due to flash heating. *J. Geophys. Res.*, *113*(B01401). doi: 10.1029/2007JB004988

Bejar Pizarro, M., Carrizo, D., Socquet, A., & Armijo, R. (2010). Asperities, barriers and transition zone in the North Chile seismic gap: State of the art after the 2007 Mw 7.7 Tocopilla earthquake inferred by GPS and InSAR data. In *Esa special publication* (Vol. 677).

Bekaert, D., Hooper, A., & Wright, T. (2015). Reassessing the 2006 Guerrero slow-slip event, Mexico: Implications for large earthquakes in the Guerrero Gap. *J. Geophys. Res.*, *120*(2), 1357–1375. doi: 10.1002/2014JB011557

Ben-Zion, Y. (2001). On quantification of the earthquake source. *Seism. Res. Lett.*, *72*(2), 151–

152. doi: 10.1785/gssrl.72.2.151

Ben-Zion, Y., Lee, W., Kanamori, H., Jennings, P., & Kisslinger, C. (2003). Key formulas in earthquake seismology. *International handbook of earthquake and engineering seismology*, *81*.

Ben-Zion, Y., & Lyakhovsky, V. (2019). Representation of seismic sources sustaining changes of elastic moduli. *Geophys. J. Int.*, *217*(1), 135–139. doi: 10.1093/gji/ggz018

Ben-Zion, Y., & Zhu, L. (2002). Potency-magnitude scaling relations for southern california earthquakes with 1.0< m_l <7.0. *Geophys. J. Int.*, *148*(3), F1–F5. doi: 10.1046/j.1365-246X .2002.01637.x

Beroza, G. C., & Ide, S. (2011). Slow Earthquakes and Nonvolcanic Tremor. *Annual Review of Earth and Planetary Sciences*, *39*(1), 271–296. doi: 10.1146/annurev-earth-040809-152531

Beroza, G. C., & Spudich, P. (1988). Linearized inversion for fault rupture behavior: Application to the 1984 Morgan Hill, California, earthquake. *J. Geophys. Res.*, *93*(B6), 6275. doi: 10 .1029/JB093iB06p06275

Bilek, S. L., Engdahl, E. R., DeShon, H. R., & El Hariri, M. (2011). The 25 October 2010 Sumatra tsunami earthquake: Slip in a slow patch. *Geophys. Res. Lett.*, *38*(L14306), 5.

Bilek, S. L., & Lay, T. (2002). Tsunami earthquakes possibly widespread manifestations of frictional conditional stability. *Geophys. Res. Lett.*, *29*(14, 1673), 4. doi: 10.1029/2002GL015215

Bletery, Q., Sladen, A., Delouis, B., Vallée, M., Nocquet, J.-m., Rolland, L., & Jiang, J. (2014). A detailed source model for the Mw 9.0 Tohoku-Oki earthquake reconciling geodesy, seismology and tsunami records. *J. Geophys. Res.*, *119*, 7636–7653. doi: 10.1002/2014JB011261

Brengman, C. M., Barnhart, W. D., Mankin, E. H., & Miller, C. N. (2019). Earthquake-scaling relationships from geodetically derived slip distributions. *Bull. Seism. Soc. Am.*, *109*(5), 1701–1715. doi: 10.1785/0120190048

Brown, L., Wang, K., & Sun, T. (2015). Static stress drop in the mw 9 tohoku-oki earthquake: Heterogeneous distribution and low average value. *Geophys. Res. Lett.*, *42*(24), 10–595. doi: 10.1002/2015GL066361

Brune, J. (1970). Tectonic stress and the spectra of seismic shear waves from earthquakes. *J. Geophys. Res.*, *75*, 4997-5009. doi: 10.1029/JB075i026p04997

Bürgmann, R. (2018). The geophysics, geology and mechanics of slow fault slip. *Earth Planet. Sci. Lett.*, *495*, 112–134. doi: 10.1016/j.epsl.2018.04.062

Cappa, F., Perrin, C., Manighetti, I., & Delor, E. (2014). Off-fault long-term damage: A condition to account for generic, triangular earthquake slip profiles. *Geochemistry, Geophysics, Geosystems*, *15*(4), 1476–1493. doi: 10.1002/2013GC005182

Cattania, C., & Segall, P. (2018). Crack models of repeating earthquakes predict observed moment-recurrence scaling. *J. Geophys. Res.*. doi: 10.1029/2018JB016056

Chen, T., & Lapusta, N. (2009). Scaling of small repeating earthquakes explained by interaction of seismic and aseismic slip in a rate and state fault model. *J. Geophys. Res.*, *114*(B01311), 12 PP. doi: 10.1029/2008JB005749

Chlieh, M., Avouac, J.-P., Hjorleifsdottir, V., Song, T.-R. A., Ji, C., Sieh, K., ... Galetzka, J. (2007, jan). Coseismic Slip and Afterslip of the Great Mw 9.15 Sumatra-Andaman Earthquake of 2004. *Bull. Seism. Soc. Am.*, *97*(1A), S152–S173. doi: 10.1785/0120050631

Chounet, A., & Vallée, M. (2018). Global and interregion characterization of subduction interface earthquakes derived from source time functions properties. *J. Geophys. Res.*, *12*(7), 5831–5852. doi: 10.1029/2018JB015932

Cocco, M., Tinti, E., & Cirella, A. (2016). On the scale dependence of earthquake stress drop. *Journal of Seismology*, *20*(4), 1151–1170. doi: 10.1007/s10950-016-9594-4

Copley, A., Avouac, J. P., Hollingsworth, J., & Leprince, S. (2011). The 2001 Mw 7.6 Bhuj earthquake, low fault friction, and the crustal support of plate driving forces in India. *J. Geophys. Res.*, *116*(8), 1–11. doi: 10.1029/2010JB008137

Courboulex, F., Vallée, M., Causse, M., & Chounet, A. (2016). Stress-drop variability of shallow earthquakes extracted from a global database of source time functions. *Seism. Res. Lett.*, *87*(4), 912–918. doi: 10.1785/0220150283

Cruz-Atienza, V. M., Villafuerte, C., & Bhat, H. S. (2018). Rapid tremor migration and pore-pressure waves in subduction zones. *Nature communications*, *9*(1), 2900. doi: 10.1038/s41467-018-05150-3

Darragh, R. B., & Bolt, B. A. (1987). *A comment on the statistical regression relation between earthquake magnitude and fault rupture length.* The Seismological Society of America.

DeVries, P. M., Krastev, P. G., Dolan, J. F., & Meade, B. J. (2017). Viscoelastic block models of the north anatolian fault: A unified earthquake cycle representation of pre-and postseismic geodetic observations. *Bull. Seism. Soc. Am.*, *107*(1), 403–417. doi: 10.1785/0120160059

Dieterich, J. H. (1979). Modeling of Rock Friction 1. Experimental Results and Constitutive Equations. *J. Geophys. Res.*, *84*(B5), 2161-2168. doi: 10.1029/JB084iB05p02161

Dixon, T. H., Jiang, Y., Malservisi, R., McCaffrey, R., Voss, N., Protti, M., & Gonzalez, V. (2014). Earthquake and tsunami forecasts: Relation of slow slip events to subsequent earthquake rupture. *Proc. Nat. Ac. Sc.*, *111*(48), 17039–17044. doi: 10.1073/pnas.1412299111

Dragert, H., & Wang, K. (2011). Temporal evolution of an episodic tremor and slip event along the northern Cascadia margin. *J. Geophys. Res.*, *116*(B12). doi: 10.1029/2011JB008609

Dreger, D. S., Gee, L., Lombard, P., Murray, M. H., & Romanowicz, B. (2005). Rapid finite-source analysis and near-fault strong ground motions: Application to the 2003 Mw 6.5 San Simeon and 2004 Mw 6.0 Parkfield earthquakes. *Seism. Res. Lett.*, *76*(1), 40–48. doi: 10.1785/gssrl.76.1.40

Duputel, Z., Agram, P. S., Simons, M., Minson, S. E., & Beck, J. L. (2014). Accounting for prediction uncertainty when inferring subsurface fault slip. *Geophys. J. Int.*, *197*(1), 464–482.

Elliott, J. R., Copley, A. C., Holley, R., Scharer, K., & Parsons, B. (2013). The 2011 Mw 7.1 Van (Eastern Turkey) earthquake. *J. Geophys. Res.*, *118*(4), 1619–1637. doi: 10.1002/jgrb.50117

Elliott, J. R., Nissen, E. K., England, P. C., Jackson, J. A., Lamb, S., Li, Z., ... Parsons, B. (2012). Slip in the 2010-2011 Canterbury earthquakes, New Zealand. *J. Geophys. Res.*, *117*(3). doi: 10.1029/2011JB008868

Elliott, J. R., Parsons, B., Jackson, J. A., Shan, X., Sloan, R. A., & Walker, R. T. (2011, mar). Depth segmentation of the seismogenic continental crust: The 2008 and 2009 Qaidam earthquakes. *Geophys. Res. Lett.*, *38*(6). doi: 10.1029/2011GL046897

Eshelby, J. D. (1957). The determination of the elastic field of an ellipsoidal inclusion, and related problems. *Proceedings of the Royal Society of London. Series A. Mathematical and*

Physical Sciences, *241*(1226), 376–396. doi: /10.1098/rspa.1957.0133

Evans, E. L., & Meade, B. J. (2012). Geodetic imaging of coseismic slip and postseismic afterslip: Sparsity promoting methods applied to the great Tohoku earthquake. *Geophys. Res. Lett.*, *39*(11). doi: 10.1029/2012GL051990

Feng, L., Hill, E. M., Elósegui, P., Qiu, Q., Hermawan, I., Banerjee, P., & Sieh, K. (2015). Hunt for slow slip events along the Sumatran subduction zone in a decade of continuous GPS data. *J. Geophys. Res.*, *120*(12), 8623–8632. doi: 10.1002/2015JB012503

Feng, W., Samsonov, S., Almeida, R., Yassaghi, A., Li, J., Qiu, Q., ... Zheng, W. (2018). Geodetic Constraints of the 2017 Mw 7.3 Sarpol Zahab, Iran Earthquake, and Its Implications on the Structure and Mechanics of the Northwest Zagros Thrust-Fold Belt. *Geophys. Res. Lett.*, *45*(14), 6853–6861. doi: 10.1029/2018GL078577

Fialko, Y. (2004). Probing the mechanical properties of seismically active crust with space geodesy: Study of the co-seismic deformation due to the 1992 M_w7.3 Landers (Southern California) earthquake. *J. Geophys. Res.*, *109*(B03307). doi: 10.1029/2003JB002756

Fialko, Y., Sandwell, D., Simons, M., & Rosen, P. (2005, May). Three-dimensional deformation caused by the Bam, Iran, earthquake and the origin of shallow slip deficit. *Nature*, *435*, 295-299. doi: 10.1038/nature03425

Fialko, Y., Simons, M., & Agnew, D. (2001). The complete (3-D) surface displacement field in the epicentral area of the 1999 M_w7.1 Hector Mine earthquake, southern California, from space geodetic observations. *Geophys. Res. Lett.*, *28*, 3063–3066. doi: 10.1029/2001GL013174

Fujiwara, T., Kodaira, S., No, T., Kaiho, Y., Takahashi, N., & Kaneda, Y. (2011). The 2011 Tohoku-Oki earthquake: Displacement reaching the trench axis. *Science*, *334*(6060), 1240–1240. doi: 10.1126/science.1211554

Fukahata, Y., & Wright, T. J. (2008). A non-linear geodetic data inversion using ABIC for slip distribution on a fault with an unknown dip angle. *Geophys. J. Int.*, *173*(2), 353–364. doi: 10.1111/j.1365-246X.2007.03713.x

Funning, G. J., Fukahata, Y., Yagi, Y., & Parsons, B. (2014). A method for the joint inversion of geodetic and seismic waveform data using ABIC: application to the 1997 Manyi, Tibet,

earthquake. *Geophys. J. Int.*, *196*(3), 1564–1579. doi: 10.1093/gji/ggt406

Gao, H., Schmidt, D. a., Ii, R. J. W., & Weldon, R. J. (2012). Scaling relationships of source parameters for slow slip events. *Bull. Seism. Soc. Am.*, *102*(1), 352–360. doi: 10.1785/0120110096

Geersen, J. (2019). Sediment-starved trenches and rough subducting plates are conducive to tsunami earthquakes. *Tectonophysics*, *762*, 28–44. doi: 10.1016/j.tecto.2019.04.024

Goldsby, D., & Tullis, T. E. (2011). Flash heating leads to low frictional strength of crustal rocks at earthquake slip rates. *Science*, *334*(6053), 216-218. doi: 10.1126/science.1207902

Gomberg, J., Wech, A., Creager, K., Obara, K., & Agnew, D. (2016, Jun). Reconsidering earthquake scaling. *Geophys. Res. Lett.*, *43*(12), 6243–6251. doi: 10.1002/2016GL069967

Gombert, B., Duputel, Z., Jolivet, R., Doubre, C., Rivera, L., & Simons, M. (2017). Revisiting the 1992 Landers earthquake: a Bayesian exploration of co-seismic slip and off-fault damage. *Geophys. J. Int.*, *212*(2), 839–852. doi: 10.1093/gji/ggx455

Gombert, B., Duputel, Z., Jolivet, R., Simons, M., Jiang, J., Liang, C., ... Rivera, L. (2018). Strain budget of the ecuador–colombia subduction zone: A stochastic view. *Earth Planet. Sci. Lett.*, *498*, 288–299.

Goodner, H. L. (2014). *Spatial relationship between gps slip and seismic tremor during cascadia slow slip events* (Unpublished doctoral dissertation). Central Washington University.

Goswami, A., & Barbot, S. (2018). Slow-slip events in semi-brittle serpentinite fault zones. *Scientific reports*, *8*(1), 6181. doi: 10.1038/s41598-018-24637-z

Gusman, A. R., Murotani, S., Satake, K., Heidarzadeh, M., Gunawan, E., Watada, S., & Schurr, B. (2015). Fault slip distribution of the 2014 Iquique, Chile, earthquake estimated from ocean-wide tsunami waveforms and GPS data. *Geophys. Res. Lett.*, *42*(4), 1053–1060. doi: 10.1002/2014GL062604

Hamling, I. J., D'Anastasio, E., Wallace, L. M., Ellis, S., Motagh, M., Samsonov, S., ... Hreinsdõttir, S. (2014). Crustal deformation and stress transfer during a propagating earthquake sequence: The 2013 Cook Strait sequence, central New Zealand. *J. Geophys. Res.*, *119*(7), 6080–6092. doi: 10.1002/2014JB011084

Hang, Y., Barbot, S., Dauwels, J., T., W., Nanjundiah, P., & Qiu, Q. (2020). Outlier-insensitive

bayesian inference for linear inverse problems (outibi) with applications to space geodetic data. *Geophys. J. Int.*, *221*, 334–350. doi: 10.1093/gji/ggz559

Hernandez, B., Cotton, F., & Campillo, M. (1999, Jun). Contribution of radar interferometry to a two-step inversion of the kinematic process of the 1992 Landers earthquake. *J. Geophys. Res.*, *104*(B6), 13083–13099. doi: 10.1029/1999JB900078

Hill, E. M., Yue, H., Barbot, S., Lay, T., Tapponnier, P., Hermawan, I., ... Sieh, K. (2015, May). The 2012 M w 8.6 Wharton Basin sequence: A cascade of great earthquakes generated by near-orthogonal, young, oceanic mantle faults. *J. Geophys. Res.*, *120*(5), 3723–3747. doi: 10.1002/2014JB011703

Hirose, T., & Bystricky, M. (2007). Extreme dynamic weakening of faults during dehydration by coseismic shear heating. *Geophys. Res. Lett.*, *34*(14). doi: 10.1029/2007GL030049

Hudnut, K., Shen, Z., Murray, M., McClusky, S., King, R., Herring, T., ... others (1996). Coseismic displacements of the 1994 Northridge, California, earthquake. *Bull. Seism. Soc. Am.*, *86*(1B), S19–S36.

Iinuma, T., Hino, R., Kido, M., Inazu, D., Osada, Y., Ito, Y., ... others (2012). Coseismic slip distribution of the 2011 off the Pacific Coast of Tohoku Earthquake (M9. 0) refined by means of seafloor geodetic data. *J. Geophys. Res.*, *117*(B7). doi: 10.1029/2012JB009186

Ishii, M., Shearer, P. M., Houston, H., & Vidale, J. E. (2005). Extent, duration and speed of the 2004 Sumatra–Andaman earthquake imaged by the Hi-Net array. *Nature*, *435*(7044), 933. doi: 10.1038/nature03675

Ji, C., Larson, K. M., Tan, Y., Hudnut, K. W., & Choi, K. (2004, Sep). Slip history of the 2003 San Simeon earthquake constrained by combining 1-Hz GPS, strong motion, and teleseismic data. *Geophys. Res. Lett.*, *31*(17). doi: 10.1029/2004GL020448

Jiang, J., & Simons, M. (2016). Probabilistic imaging of tsunamigenic seafloor deformation during the 2011 tohoku-oki earthquake. *J. Geophys. Res.*, *121*(12), 9050–9076.

Jiang, Y., Wdowinski, S., Dixon, T. H., Hackl, M., Protti, M., & Gonzalez, V. (2012). Slow slip events in Costa Rica detected by continuous GPS observations, 2002–2011. *Geochemistry, Geophysics, Geosystems*, *13*(4). doi: 10.1029/2012GC004058

Johnson, J. M., Satake, K., Holdahl, S. R., & Sauber, J. (1996). The 1964 Prince William Sound

607 earthquake: Joint inversion of tsunami and geodetic data. *J. Geophys. Res.*, *101*(B1), 523–
608 532. doi: 10.1029/95jb02806

609 Kanamori, H. (1972). Mechanism of tsunami earthquake. *Phys. Earth Planet. Inter.*, *6*, 346–359.
610 doi: 10.1016/0031-9201(72)90058-1

611 Kanamori, H., & Anderson, D. (1975). Theoretical basis for some empirical relations in seismol-
612 ogy. *Bull. Seism. Soc. Am.*, *65*(5), 213–220.

613 Kanamori, H., Mori, J. I. M., Hauksson, E., Heaton, T. H., Hutton, K., & Jones, L. M. (1993).
614 Determination of Earthquake Energy Release and ML using Terrascope. *Bull. Seism. Soc.*
615 *Am.*, *83*(2), 330–346.

616 Kanamori, H., & Rivera, L. (2006). Energy partitioning during an earthquake. In R. Abercrom-
617 bie, A. McGarr, A. Kanamori, & G. D. Toro (Eds.), *Earthquakes: Radiated energy and the*
618 *physics of faulting* (Vol. 170, p. 3-13). Washington D.C.: AGU.

619 Kaneko, Y., Avouac, J.-P., & Lapusta, N. (2010). Towards inferring earthquake patterns from
620 geodetic observations of interseismic coupling. *Nature Geoscience*, *3*, 363-369. doi: 10.1038/
621 ngeo843

622 Kaneko, Y., & Shearer, P. (2014). Seismic source spectra and estimated stress drop derived from
623 cohesive-zone models of circular subshear rupture. *Geophys. J. Int.*, *197*(2), 1002–1015. doi:
624 10.1093/gji/ggu030

625 Kaneko, Y., & Shearer, P. (2015). Variability of seismic source spectra, estimated stress
626 drop, and radiated energy, derived from cohesive-zone models of symmetrical and asym-
627 metrical circular and elliptical ruptures. *J. Geophys. Res.*, *120*(2), 1053–1079. doi:
628 10.1002/2014JB011642

629 Kato, N. (2012). Dependence of earthquake stress drop on critical slip-weakening distance. *J.*
630 *Geophys. Res.*, *117*(B1). doi: 10.1029/2011JB008359

631 Kirkpatrick, J., & Shipton, Z. (2009). Geologic evidence for multiple slip weakening mecha-
632 nisms during seismic slip in crystalline rock. *J. Geophys. Res.*, *114*(B12). doi: 10.1029/
633 2008JB006037

634 Kitajima, H., Chester, F. M., & Chester, J. S. (2011). Dynamic weakening of gouge layers
635 in high-speed shear experiments: Assessment of temperature-dependent friction, thermal

pressurization, and flash heating. *J. Geophys. Res.*, *116*(B8). doi: 10.1029/2010JB007879

Konca, A. O., Hjorleifsdottir, V., Song, T.-R. A., Avouac, J.-P., Helmberger, D. V., Ji, C., ... Meltzner, A. (2007). Rupture kinematics of the 2005 Mw 8.6 Nias–Simeulue earthquake from the joint inversion of seismic and geodetic data. *Bull. Seism. Soc. Am.*, *97*(1A), S307–S322. doi: 10.1785/0120050632

Lapusta, N., & Barbot, S. (2012). Models of earthquakes and aseismic slip based on laboratory-derived rate and state friction laws. In A. Bizzarri & H. S. Bhat (Eds.), *The mechanics of faulting: From laboratory to real earthquakes* (p. 153-207). Trivandrum, Kerala, India: Research Signpost.

Lasserre, C., Peltzer, G., Crampé, F., Klinger, Y., Van der Woerd, J., & Tapponnier, P. (2005). Coseismic deformation of the 2001 Mw=7.8 Kokoxili earthquake in Tibet, measured by synthetic aperture radar interferometry. *J. Geophys. Res.*, *110*(B12), B12408. doi: 10.1029/2004JB003500

Leeman, J., Saffer, D., Scuderi, M., & Marone, C. (2016). Laboratory observations of slow earthquakes and the spectrum of tectonic fault slip modes. *Nature communications*, *7*, 11104. doi: 10.1038/ncomms11104

Li, Z., Elliott, J. R., Feng, W., Jackson, J. A., Parsons, B. E., & Walters, R. J. (2011). The 2010 MW 6.8 Yushu (Qinghai, China) earthquake: Constraints provided by InSAR and body wave seismology. *J. Geophys. Res.*, *116*(B10). doi: 10.1029/2011JB008358

Liu, Y., & Rice, J. R. (2005). Aseismic slip transients emerge spontaneously in three-dimensional rate and state modeling of subduction earthquake sequences. *J. Geophys. Res.*, *110*(B08307). doi: 10.1029/2004JB003424

Liu, Y., & Rice, J. R. (2007). Spontaneous and triggered aseismic deformation transients in a subduction fault model. *J. Geophys. Res.*, *112*(B09404). doi: 10.1029/2007JB004930

Liu-Zeng, J., Heaton, T., & DiCaprio, C. (2005). The effect of slip variability on earthquake slip-length scaling. *Geophys. J. Int.*, *162*(3), 841–849. doi: 10.1111/j.1365-246X.2005.02679.x

Lorenzo-Martín, F., Roth, F., & Wang, R. (2006). Inversion for rheological parameters from post-seismic surface deformation associated with the 1960 Valdivia earthquake, Chile. *Geophys. J. Int.*, *164*(1), 75–87. doi: 10.1111/j.1365-246X.2005.02803.x

Lorito, S., Romano, F., Atzori, S., Tong, X., Avallone, A., McCloskey, J., ... Piatanesi, A. (2011). Limited overlap between the seismic gap and coseismic slip of the great 2010 Chile earthquake. *Nature Geoscience*, *4*(3), 173–177. doi: 10.1038/ngeo1073

Loveless, J. P., & Meade, B. J. (2011). Spatial correlation of interseismic coupling and coseismic rupture extent of the 2011 Mw= 9.0 Tohoku-oki earthquake. *Geophys. Res. Lett.*, *38*(17). doi: 10.1029/2011GL048561

Luttrell, K. M., Tong, X., Sandwell, D. T., Brooks, B. A., & Bevis, M. G. (2011). Estimates of stress drop and crustal tectonic stress from the 27 February 2010 Maule, Chile, earthquake: Implications for fault strength. *J. Geophys. Res.*, *116*(B11). doi: 10.1029/2011JB008509

Madariaga, R. (1976). Dynamics of an expanding circular fault. *Bull. Seism. Soc. Am.*, *66*(3), 639–666.

Madariaga, R. (1977). Implications of stress-drop models of earthquakes for the inversion of stress drop from seismic observations. In *Stress in the earth* (pp. 301–316). Springer. doi: 10.1007/978-3-0348-5745-1_19

Mai, P. M., & Beroza, G. C. (2000). Source scaling properties from finite-fault-rupture models. *Bull. Seism. Soc. Am.*, *90*(3), 604–615. doi: 10.1785/0119990126

Manighetti, I., Campillo, M., Bouley, S., & Cotton, F. (2007). Earthquake scaling, fault segmentation, and structural maturity. *Earth Planet. Sci. Lett.*, *253*(3-4), 429–438. doi: 10.1016/j.epsl.2006.11.004

Manighetti, I., King, G., Gaudemer, Y., Scholz, C., & Doubre, C. (2001). Slip accumulation and lateral propagation of active normal faults in Afar. *J. Geophys. Res.*, *106*, 13667-13696. doi: 10.1029/2000JB900471

McGuire, J. J., & Segall, P. (2003). Imaging of aseismic fault slip transients recorded by dense geodetic networks. *Geophys. J. Int.*, *155*, 778-788. doi: 10.1111/j.1365-246X.2003.02022.x

Michel, S., Avouac, J.-P., Lapusta, N., & Jiang, J. (2017). Pulse-like partial ruptures and high-frequency radiation at creeping-locked transition during megathrust earthquakes. *Geophys. Res. Lett.*, *44*(16), 8345–8351. doi: 10.1002/2017GL074725

Michel, S., Gualandi, A., & Avouac, J.-P. (2019). Similar scaling laws for earthquakes and Cascadia slow-slip events. *Nature*, *574*(7779), 522–526. doi: 10.1038/s41586-019-1673-6

Minson, S. E., Simons, M., Beck, J. L., Ortega, F., Jiang, J., Owen, S. E., ... Sladen, A. (2014). Bayesian inversion for finite fault earthquake source models - II: The 2011 great Tohoku-oki, Japan earthquake. *Geophys. J. Int.*, *198*(2), 922–940. doi: 10.1093/gji/ggu170

Mitsui, Y., Iio, Y., & Fukahata, Y. (2012). A scenario for the generation process of the 2011 Tohoku earthquake based on dynamic rupture simulation: role of stress concentration and thermal fluid pressurization. *Earth Planet. Sp.*, *64*(12), 12. doi: 10.5047/eps.2012.05.016

Miyakoshi, K., Somei, K., Yoshida, K., Kurahashi, S., Irikura, K., & Kamae, K. (2019). Scaling relationships of source parameters of inland crustal earthquakes in tectonically active regions. *Pure and Applied Geophysics*, 1–13. doi: 10.1007/s00024-019-02160-0

Moore, J. D., Yu, H., Tang, C.-H., Wang, T., Barbot, S., Peng, D., ... others (2017). Imaging the distribution of transient viscosity after the 2016 Mw 7.1 Kumamoto earthquake. *Science*, *356*(6334), 163–167. doi: 10.1126/science.aal3422

Moreno, M. S., Bolte, J., Klotz, J., & Melnick, D. (2009). Impact of megathrust geometry on inversion of coseismic slip from geodetic data: Application to the 1960 Chile earthquake. *Geophys. Res. Lett.*, *36*(16). doi: 10.1029/2009GL039276

Nakano, M., Hori, T., Araki, E., Kodaira, S., & Ide, S. (2018). Shallow very-low-frequency earthquakes accompany slow slip events in the Nankai subduction zone. *Nature communications*, *9*(1), 984. doi: 10.1038/s41467-018-03431-5

Nemat-Nasser, S. (2004). *Plasticity. a treatise on finite deformation of heterogeneous inelastic materials.* Cambridge University Press.

Nemat-Nasser, S., & Hori, M. (1999). *Micromechanics: overall properties of heterogeneous materials* (2nd ed.). Elsevier. doi: 10.1115/1.2788912

Newman, A. V., Feng, L., Fritz, H. M., Lifton, Z. M., Kalligeris, N., & Wei, Y. (2011). The energetic 2010 MW 7.1 Solomon Islands tsunami earthquake. *Geophys. J. Int.*, *186*(2), 775–781. doi: 10.1111/j.1365-246X.2011.05057.x

Newman, A. V., Hayes, G., Wei, Y., & Convers, J. (2011). The 25 October 2010 Mentawai tsunami earthquake, from real-time discriminants, finite-fault rupture, and tsunami excitation. *Geophys. Res. Lett.*, *38*(L05302), 7. doi: 10.1029/2010GL046498

Nikkhoo, M., & Walter, T. R. (2015). Triangular dislocation: an analytical, artefact-free solution.

Geophys. J. Int., *201*(2), 1119–1141. doi: 10.1093/gji/ggv035

Nocquet, J.-M. (2018). Stochastic static fault slip inversion from geodetic data with non-negativity and bound constraints. *Geophysical Journal International*, *214*(1), 366–385. doi: 10.1093/gji/ggy146

Noda, H., & Lapusta, N. (2013). Stable creeping fault segments can become destructive as a result of dynamic weakening. *Nature*, *493*(7433), 518–521. doi: 10.1038/nature11703

Noda, H., Lapusta, N., & Kanamori, H. (2013). Comparison of average stress drop measures for ruptures with heterogeneous stress change and implications for earthquake physics. *Geophys. J. Int.*, *193*(3), 1691–1712. doi: 10.1093/gji/ggt074

Obara, K., & Kato, A. (2016). Connecting slow earthquakes to huge earthquakes. *Science*, *353*(6296), 253–258. doi: 10.1126/science.aaf1512

Okada, Y. (1992). Internal deformation due to shear and tensile faults in a half-space. *Bull. Seism. Soc. Am.*, *82*(2), 1018–1040.

Pelayo, A. M., & Wiens, D. A. (1992). Tsunami earthquakes: Slow thrust-faulting events in the accretionary wedge. *J. Geophys. Res.*, *97*(B11), 15321–15337. doi: 10.1029/92JB01305

Peng, Z., & Gomberg, J. (2010). An integrated perspective of the continuum between earthquakes and slow-slip phenomena. *Nature Geoscience*, *3*(9), 599. doi: 10.1038/ngeo940

Poli, P., & Prieto, G. A. (2016). Global rupture parameters for deep and intermediate-depth earthquakes. *J. Geophys. Res.*, *121*(12), 8871–8887. doi: 10.1002/2016JB013521

Prieto, G. A., Parker, R. L., Vernon, F. L., Shearer, P. M., Thomson, D. J., Abercrombie, R., & McGarr, A. (2006). Uncertainties in earthquake source spectrum estimation using empirical green functions. *Geophys. Monograph - Am. Geophys. Union*, *170*, 69. doi: 10.1029/170GM08

Qiu, Q., Hill, E. M., Barbot, S., Hubbard, J., Feng, W., Lindsey, E. O., ... Tapponnier, P. (2016). The mechanism of partial rupture of a locked megathrust: The role of fault morphology. *Geology*, *44*(10), 875–878. doi: 10.1130/G38178.1

Radiguet, M., Cotton, F., Vergnolle, M., Campillo, M., Walpersdorf, A., Cotte, N., & Kostoglodov, V. (2012, apr). Slow slip events and strain accumulation in the Guerrero gap, Mexico. *J. Geophys. Res.*, *117*(B4). doi: 10.1029/2011JB008801

Rhie, J., Dreger, D., Bürgmann, R., & Romanowicz, B. (2007). Slip of the 2004 Sumatra-Andaman earthquake from joint inversion of long-period global seismic waveforms and GPS static offsets. *Bull. Seism. Soc. Am.*, *97*(1A), S115–S127. doi: 10.1785/0120050620

Romanowicz, B. (1992). Strike-slip earthquakes on quasi-vertical transcurrent faults: Inferences for general scaling relations. *Geophys. Res. Lett.*, *19*(5), 481–484. doi: 10.1029/92GL00265

Ruina, A. (1983). Slip instability and state variable friction laws. *J. Geophys. Res.*, *88*, 10,359–10,370. doi: 10.1029/JB088iB12p10359

Salichon, J., Lundgren, P., Delouis, B., & Giardini, D. (2004). Slip history of the 16 October 1999 Mw 7.1 Hector Mine earthquake (California) from the inversion of InSAR, GPS, and teleseismic data. *Bull. Seism. Soc. Am.*, *94*(6), 2015–2027. doi: 10.1785/0120030038

Sallarès, V., & Ranero, C. R. (2019). Upper-plate rigidity determines depth-varying rupture behaviour of megathrust earthquakes. *Nature*, *576*(7785), 96–101. doi: 10.1038/s41586-019-1784-0

Salman, R., Hill, E. M., Feng, L., Lindsey, E. O., Mele Veedu, D., Barbot, S., ... Natawidjaja, D. H. (2017). Piecemeal Rupture of the Mentawai Patch, Sumatra: The 2008 Mw 7.2 North Pagai Earthquake Sequence. *J. Geophys. Res.*, *122*(11), 9404–9419. doi: 10.1002/2017JB014341

Satake, K., Nishimura, Y., Putra, P. S., Gusman, A. R., Sunendar, H., Fujii, Y., ... Yulianto, E. (2013). Tsunami source of the 2010 Mentawai, Indonesia earthquake inferred from tsunami field survey and waveform modeling. *Pure Appl. Geophys.*, *170*(9-10), 1567–1582. doi: 10.1007/s00024-012-0536-y

Satake, K., & Tanioka, Y. (1999). Sources of tsunami and tsunamigenic earthquakes in subduction zones. *Pure Appl. Geophys.*, *154*(3-4), 467–483. doi: 10.1007/s000240050240

Sathiakumar, S., Barbot, S., & Hubbard, J. (2019). Seismic cycles in fault-bend folds. *subm. to J. Geophys. Res.*. doi: 10.1029/2019JB018557

Sathiakumar, S., Barbot, S. D., & Agram, P. (2017). Extending resolution of fault slip with geodetic networks through optimal network design. *J. Geophys. Res.*, *122*(12). doi: 10.1029/2019JB018557

Schmidt, D. A., & Gao, H. (2010, apr). Source parameters and time-dependent slip distributions

of slow slip events on the Cascadia subduction zone from 1998 to 2008. *J. Geophys. Res.*, *115*, B00A18. doi: 10.1029/2008JB006045

Scholz, C. H. (1998, January). Earthquakes and friction laws. *Nature*, *391*, 37-42. doi: 10.1038/34097

Scholz, C. H., Aviles, C., & Wesnousky, S. G. (1986). Scaling differences between large interplate and intraplate earthquakes. *Bull. Seism. Soc. Am.*, *76*(1), 65–70.

Scuderi, M. M., Collettini, C., Viti, C., Tinti, E., & Marone, C. (2017). Evolution of shear fabric in granular fault gouge from stable sliding to stick slip and implications for fault slip mode. *Geology*, *45*(8), 731–734. doi: 10.1130/G39033.1

Segall, P., Rubin, A. M., Bradley, A. M., & Rice, J. R. (2010). Dilatant strengthening as a mechanism for slow slip events. *J. Geophys. Res.*, *115*(B12305). doi: 10.1029/2010JB007449

Shearer, P. M., Prieto, G. A., & Hauksson, E. (2006). Comprehensive analysis of earthquake source spectra in southern California. *J. Geophys. Res.*, *111*(B6). doi: 10.1029/2005JB003979

Shi, Q., Barbot, S., Shibazaki, B., Matsuzawa, T., Wei, S., & Tapponnier, P. (2020). Structural control and system-level behavior of the seismic cycle at the Nankai trough. *Earth Planet. Sp.*, *72*(1), 1–31. doi: 10.1186/s40623-020-1145-0

Simons, M. (2002). Coseismic Deformation from the 1999 Mw 7.1 Hector Mine, California, Earthquake as Inferred from InSAR and GPS Observations. *Bull. Seism. Soc. Am.*, *92*(4), 1390–1402. doi: 10.1785/0120000933

Simons, M., Minson, S., Sladen, A., Ortega, F., Jiang, J., Owen, S. E., ... Webb, F. H. (2012). The 2011 Magnitude 9.0 Tohoku-Oki Earthquake: Mosaicking the Megathrust from Seconds to Centuries. *Science*, *332*(6036), 1421-1425. doi: 10.1126/science.1206731

Somerville, P., Irikura, K., Graves, R., Sawada, S., Wald, D., Abrahamson, N., ... Kowada, A. (1999). Characterizing crustal earthquake slip models for the prediction of strong ground motion. *Seism. Res. Lett.*, *70*(1), 59–80. doi: 10.1785/gssrl.70.1.59

Song, S. G., Beroza, G. C., & Segall, P. (2008). A unified source model for the 1906 San Francisco earthquake. *Bull. Seism. Soc. Am.*, *98*(2), 823–831. doi: 10.1785/0120060402

Steblov, G. M., Kogan, M. G., Levin, B. V., Vasilenko, N. F., Prytkov, A. S., & Frolov, D. I.

(2008). Spatially linked asperities of the 2006–2007 great Kuril earthquakes revealed by GPS. *Geophys. Res. Lett.*, *35*(22). doi: 10.1029/2008GL035572

Symithe, S. J., Calais, E., Haase, J. S., Freed, A. M., & Douilly, R. (2013). Coseismic slip distribution of the 2010 M 7.0 Haiti earthquake and resulting stress changes on regional faults. *Bull. Seism. Soc. Am.*, *103*(4), 2326–2343. doi: 10.1785/0120120306

Tarantola, A. (2004). *Inverse Problem Theory*. doi: 10.1137/1.9780898717921

Thomas, M. Y., Avouac, J. P., Gratier, J. P., & Lee, J. C. (2014). Lithological control on the deformation mechanism and the mode of fault slip on the Longitudinal Valley Fault, Taiwan. *Tectonophysics*, *632*(C), 48–63. doi: 10.1016/j.tecto.2014.05.038

Toh, A., Obana, K., & Araki, E. (2018). Distribution of very low frequency earthquakes in the Nankai accretionary prism influenced by a subducting-ridge. *Earth and Planetary Science Letters*, *482*, 342–356. doi: 10.1016/j.epsl.2017.10.062

Toksoz, M., Reilinger, R., Doll, C., Barka, A., & Yalcin, N. (1999). Izmit (Turkey) earthquake of 17 August 1999: first report. *Seism. Res. Lett.*, *70*(6), 669–679. doi: 10.1785/gssrl.70.6.669

Tomita, F., Kido, M., Ohta, Y., Iinuma, T., & Hino, R. (2017). Along-trench variation in seafloor displacements after the 2011 Tohoku earthquake. *Science advances*, *3*(7), e1700113. doi: 10.1126/sciadv.1700113

Toro, G. D., Goldsby, D. L., & Tullis, T. E. (2004). Friction falls towards zero in quartz rock as slip velocity approaches seismic rates. *Nature*, *427*, 436-439. doi: 10.1038/nature02249

Toro, G. D., Hirose, T., Nielsen, S., Pennacchioni, G., & Shimamoto, T. (2006). Natural and experimental evidence of melt lubrication of faults during earthquakes. *Science*, *311*(5761), 647-649. doi: 10.1126/science.1121012

Tsang, L. L. H., Hill, E. M., Barbot, S., Qiu, Q., Feng, L., Hermawan, I., ... Natawidjaja, D. H. (2016, Dec). Afterslip following the 2007 M w 8.4 Bengkulu earthquake in Sumatra loaded the 2010 M w 7.8 Mentawai tsunami earthquake rupture zone. *J. Geophys. Res.*, *121*(12), 9034–9049. doi: 10.1002/2016JB013432

Vallée, M. (2013). Source time function properties indicate a strain drop independent of earthquake depth and magnitude. *Nature communications*, *4*, 2606.

Veedu, D. M., & Barbot, S. (2016). The Parkfield tremors reveal slow and fast ruptures on the same asperity. *Nature*, *1385*(2010), 23765. Retrieved from `http://dx.doi.org/10.1038/nature17190` doi: 10.1038/nature17190

Venkataraman, A., & Kanamori, H. (2004). Observational constraints on the fracture energy of subduction zone earthquakes. *J. Geophys. Res.*, *109*(B5). doi: 10.1029/2003JB002549

Viesca, R. C., & Garagash, D. I. (2015). Ubiquitous weakening of faults due to thermal pressurization. *Nature Geoscience*, *8*(11), 875. doi: 10.1038/ngeo2554

Wald, D. J., & Heaton, T. H. (1994). Spatial and temporal distribution of slip for the 1992 Landers, California earthquake. *Bull. Seism. Soc. Am.*, *84*(3), 668–691.

Wallace, L. M., Araki, E., Saffer, D., Wang, X., Roesner, A., Kopf, A., ... others (2016). Near-field observations of an offshore Mw 6.0 earthquake from an integrated seafloor and subseafloor monitoring network at the Nankai Trough, southwest Japan. *J. Geophys. Res.*, *121*(11), 8338–8351. doi: 10.1002/2016JB013417

Wallace, L. M., & Eberhart-Phillips, D. (2013). Newly observed, deep slow slip events at the central Hikurangi margin, New Zealand: Implications for downdip variability of slow slip and tremor, and relationship to seismic structure. *Geophys. Res. Lett.*, *40*(20), 5393–5398. doi: 10.1002/2013GL057682

Wallace, L. M., Kaneko, Y., Hreinsdóttir, S., Hamling, I., Peng, Z., Bartlow, N., ... Fry, B. (2017). Large-scale dynamic triggering of shallow slow slip enhanced by overlying sedimentary wedge. *Nature Geoscience*, *10*(10), 765. doi: 10.1038/ngeo3021

Walsh, J. J., & Watterson, J. (1988). Analysis of the relationship between displacements and dimensions of faults. *Journal of Structural geology*, *10*(3), 239–247. doi: 10.1016/0191-8141(88)90057-0

Wang, H., Xu, C., & Ge, L. (2007, Oct). Coseismic deformation and slip distribution of the 1997 7.5 Manyi, Tibet, earthquake from InSAR measurements. *Journal of Geodynamics*, *44*(3-5), 200–212. doi: 10.1016/j.jog.2007.03.003

Wang, T., & Jónsson, S. (2015). Improved sar amplitude image offset measurements for deriving three-dimensional coseismic displacements. *IEEE Journal of Selected Topics in Applied Earth Observations and Remote Sensing*, *8*(7), 3271–3278. doi: 10.1109/JSTARS.2014

.2387865

Wang, T., Shi, Q., Nikkhoo, M., Wei, S., Barbot, S., Dreger, D., ... Chen, Q.-F. (2018). The rise, collapse, and compaction of mt. mantap from the 3 september 2017 north korean nuclear test. *Science*, eaar7230. doi: 10.1126/science.aar7230

Wang, T., Wei, S., Shi, X., Qiu, Q., Li, L., Peng, D., ... Barbot, S. (2018). The 2016 Kaikōura earthquake: Simultaneous rupture of the subduction interface and overlying faults. *Earth Planet. Sci. Lett.*, *482*, 44–51. doi: 10.1016/j.epsl.2017.10.056

Wang, Y., Lin, Y.-N. N., Simons, M., & Tun, S. T. (2014, dec). Shallow Rupture of the 2011 Tarlay Earthquake (Mw 6.8), Eastern Myanmar. *Bull. Seism. Soc. Am.*, *104*(6), 2904–2914. Retrieved from `https://pubs.geoscienceworld.org/bssa/article/104/6/2904-2914/331895` doi: 10.1785/0120120364

Wang, Z., Zhang, R., Wang, X., & Liu, G. (2018). Retrieving three-dimensional co-seismic deformation of the 2017 MW7. 3 Iraq earthquake by multi-sensor SAR images. *Remote Sensing*, *10*(6), 857.

Wei, M., Sandwell, D., Fialko, Y., & Bilham, R. (2011). Slip on faults in the Imperial Valley triggered by the 4 April 2010 Mw 7.2 El Mayor-Cucapah earthquake revealed by InSAR. *Geophys. Res. Lett.*, *38*(1). doi: 10.1029/2010GL045235

Wei, S., Barbot, S., Graves, R., Lienkaemper, J. J., Wang, T., Hudnut, K., ... Helmberger, D. (2014). The 2014 Mw 6.1 South Napa Earthquake: A Unilateral Rupture with Shallow Asperity and Rapid Afterslip. *Seism. Res. Lett.*, *86*(2A), 344–354. doi: 10.1785/0220140249

Wei, S., Barbot, S., Graves, R., Lienkaemper, J. J., Wang, T., Hudnut, K., ... Helmberger, D. (2015). The 2014 Mw 6.1 South Napa Earthquake: A Unilateral Rupture with Shallow Asperity and Rapid Afterslip. *Seism. Res. Lett.*, *86*(2A), 344–354. doi: 10.1785/0220140249

Wei, S., Chen, M., Wang, X., Graves, R., Lindsey, E., Wang, T., ... Helmberger, D. (2018). The 2015 Gorkha (Nepal) earthquake sequence: I. Source modeling and deterministic 3D ground shaking. *Tectonophysics*, *722*, 447–461. doi: 10.1016/j.tecto.2017.11.024

Wei, S., Graves, R., Helmberger, D., Avouac, J. P., & Jiang, J. (2012). Sources of shaking and flooding during the Tohoku-Oki earthquake: A mixture of rupture styles. *Earth Planet. Sci. Lett.*, *333-334*, 91–100. doi: 10.1016/j.epsl.2012.04.006

Wei, S., Helmberger, D., & Avouac, J.-p. (2013, jul). Modeling the 2012 Wharton basin earthquakes off-Sumatra: Complete lithospheric failure. *J. Geophys. Res.*, *118*(7), 3592–3609. doi: 10.1002/jgrb.50267

Wells, D. L., & Coppersmith, K. J. (1994). New empirical relationships among magnitude, rupture length, rupture width, rupture area, and surface displacement. *Bull. Seism. Soc. Am.*, *84*(4), 975-1002.

Weston, J., Ferreira, A. M., & Funning, G. J. (2012). Systematic comparisons of earthquake source models determined using insar and seismic data. *Tectonophysics*, *532*, 61–81. doi: 10.1016/j.tecto.2012.02.001

Wyss, M. (1979). Estimating maximum expectable magnitude of earthquakes from fault dimensions. *Geology*, *7*(7), 336–340. doi: 10.1130/0091-7613(1979)7⟨336:EMEMOE⟩2.0.CO;2

Yabuki, T., & Matsu'ura, M. (1992). Geodetic data inversion using a bayesian information criterion for spatial distribution of fault slip. *Geophysical Journal International*, *109*(2), 363–375. doi: 10.1111/j.1365-246X.1992.tb00102.x

Yamazaki, Y., Lay, T., Cheung, K. F., Yue, H., & Kanamori, H. (2011). Modeling near-field tsunami observations to improve finite-fault slip models for the 11 March 2011 Tohoku earthquake. *Geophys. Res. Lett.*, *38*(7), n/a–n/a. doi: 10.1029/2011GL049130

Ye, L., Lay, T., Kanamori, H., & Rivera, L. (2016a). Rupture characteristics of major and great (M w $\geq$ 7.0) megathrust earthquakes from 1990 to 2015: 1. Source parameter scaling relationships. *J. Geophys. Res.*, *121*(2), 826–844. doi: 10.1002/2015JB012426

Ye, L., Lay, T., Kanamori, H., & Rivera, L. (2016b). Rupture characteristics of major and great (Mw$\geq$7.0) megathrust earthquakes from 1990 to 2015: 2. Depth dependence Lingling. *J. Geophys. Res.*, 845–863. doi: 10.1002/2015JB012426.Rupture

Yu, S.-B., Kuo, L.-C., Hsu, Y.-J., Su, H.-H., Liu, C.-C., Hou, C.-S., ... others (2001). Preseismic deformation and coseismic displacements associated with the 1999 Chi-Chi, Taiwan, earthquake. *Bull. Seism. Soc. Am.*, *91*(5), 995–1012. doi: 10.1785/0120000722

Yue, H., Lay, T., Rivera, L., An, C., Vigny, C., Tong, X., & Báez Soto, J. C. (2014). Localized fault slip to the trench in the 2010 Maule, Chile Mw= 8.8 earthquake from joint inversion of high-rate GPS, teleseismic body waves, InSAR, campaign GPS, and tsunami observa-

tions. *J. Geophys. Res.*, *119*(10), 7786–7804. doi: 10.1002/2014JB011340

Yue, H., Lay, T., Rivera, L., Bai, Y., Yamazaki, Y., Cheung, K. F., ... Muhari, A. (2014). Rupture process of the 2010 M w 7.8 Mentawai tsunami earthquake from joint inversion of near-field hr-GPS and teleseismic body wave recordings constrained by tsunami observations. *J. Geophys. Res.*, *119*(7), 5574–5593. doi: 10.1002/2014JB011082

Yue, H., Lay, T., Schwartz, S. Y., Rivera, L., Protti, M., Dixon, T. H., ... Newman, A. V. (2013). The 5 September 2012 Nicoya, Costa Rica M w 7.6 earthquake rupture process from joint inversion of high-rate GPS, strong-motion, and teleseismic P wave data and its relationship to adjacent plate boundary interface properties. *J. Geophys. Res.*, *118*(10), 5453–5466. doi: 10.1002/jgrb.50379

Zeng, Y., & Anderson, J. G. (2000). *Evaluation of numerical procedures for simulating near-fault long-period ground motions using Zeng method.* Pacific Earthquake Engineering Research Center.

Zigone, D., Rivet, D., Radiguet, M., Campillo, M., Voisin, C., Cotte, N., ... others (2012). Triggering of tremors and slow slip event in guerrero, mexico, by the 2010 mw 8.8 maule, chile, earthquake. *J. Geophys. Res.*, *117*(B9).